Anatoly Balagurov
Frank Laboratory of Neutron Physics

Neutron Diffraction for Solid State Physics and Materials Science

- Variety of neutron diffractometers
- Complementarity of λ = const и TOF-diffractometers
- Basic neutron diffraction tasks
- Neutron diffraction at the IBR-2 pulsed reactor
  - instruments
  - high-resolution mode – atomic & magnetic structures
  - high-intensity mode – irreversible processes
  - applied studies

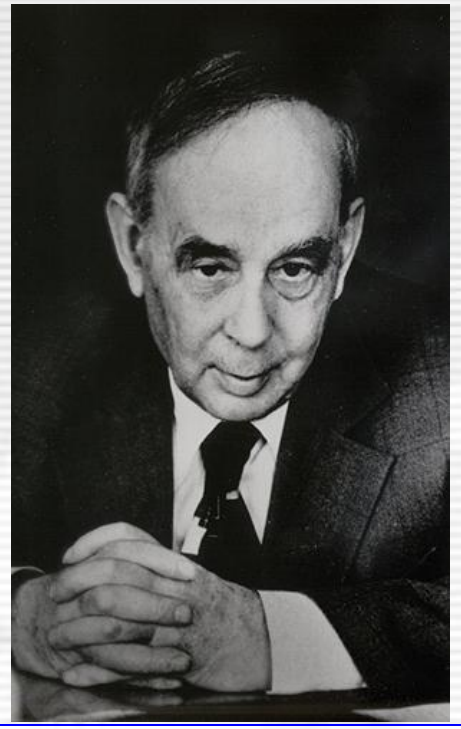

I. M. Frank, 1908 – 1990

Nobel prize winner (1958)

Director of the Laboratory of Neutron Physics, 1956 - 1990

bala@nf.jinr.ru

Neutron Scattering for Condensed Matter Science

Neutron scattering is a set of experimental methods for studying the structure and dynamic of condensed matter at the atomic or molecular level by using low-energy neutrons with a characteristic energy of ~0.02 eV and wavelength of ~2 Å.

<u>Its special features are</u>: sensitivity to light atoms, sensitivity to isotope content, strong magnetic interaction, high penetration depth, large size of beam cross-section.

Main topics:		Basic techniques:
- atomic and magnetic structures	→	- diffraction
- atomic and magnetic dynamics	→	- inelastic scattering
- large-scale inhomogeneities	→	- small angle scattering
- multilayers and interfaces	→	- reflectometry
- applied research	→	- diffraction & imaging

Steady state research reactor, W = 10 – 100 MW, Const in time

ILL, France
FRM II, Germany
NIST, USA
ORNL, USA
CARR, China
PIK, Russia

IAEA data: ~200 reactors

The FRM-II complex (Munich, Germany) includes 2 reactors and experimental halls.

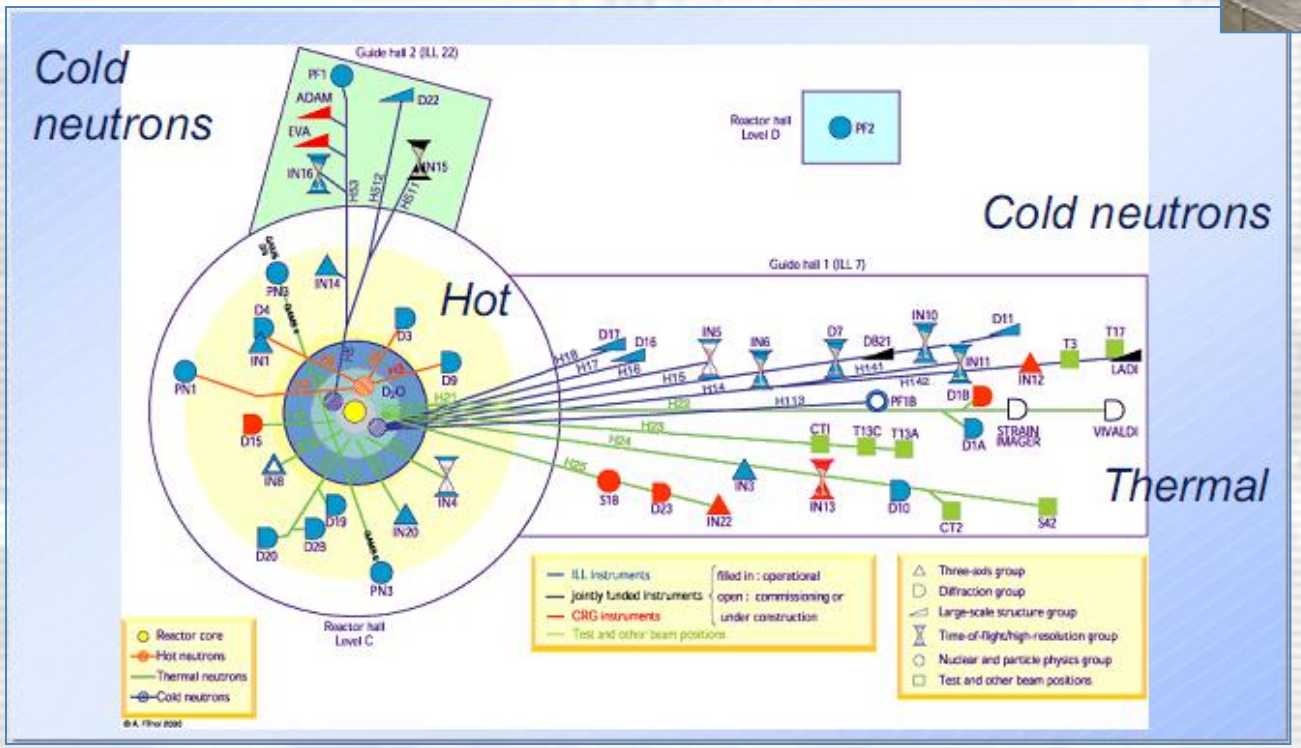

Schematic diagram of the neutron spectrometer complex around the ILL reactor (Grenoble, France).

The complex includes spectrometers at hot, thermal and cold neutron sources (>40 altogether).

Pulsed neutron sources

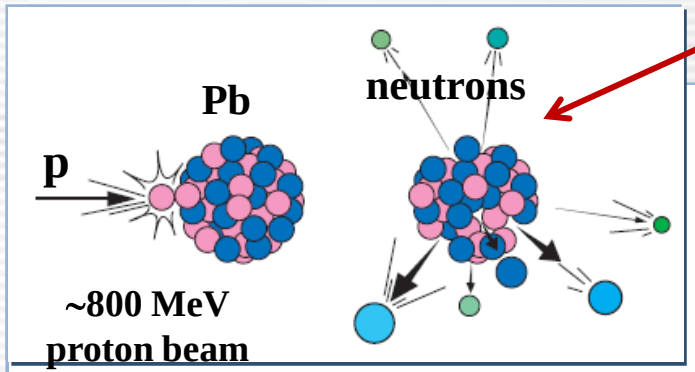

Spallation (evaporation) reaction

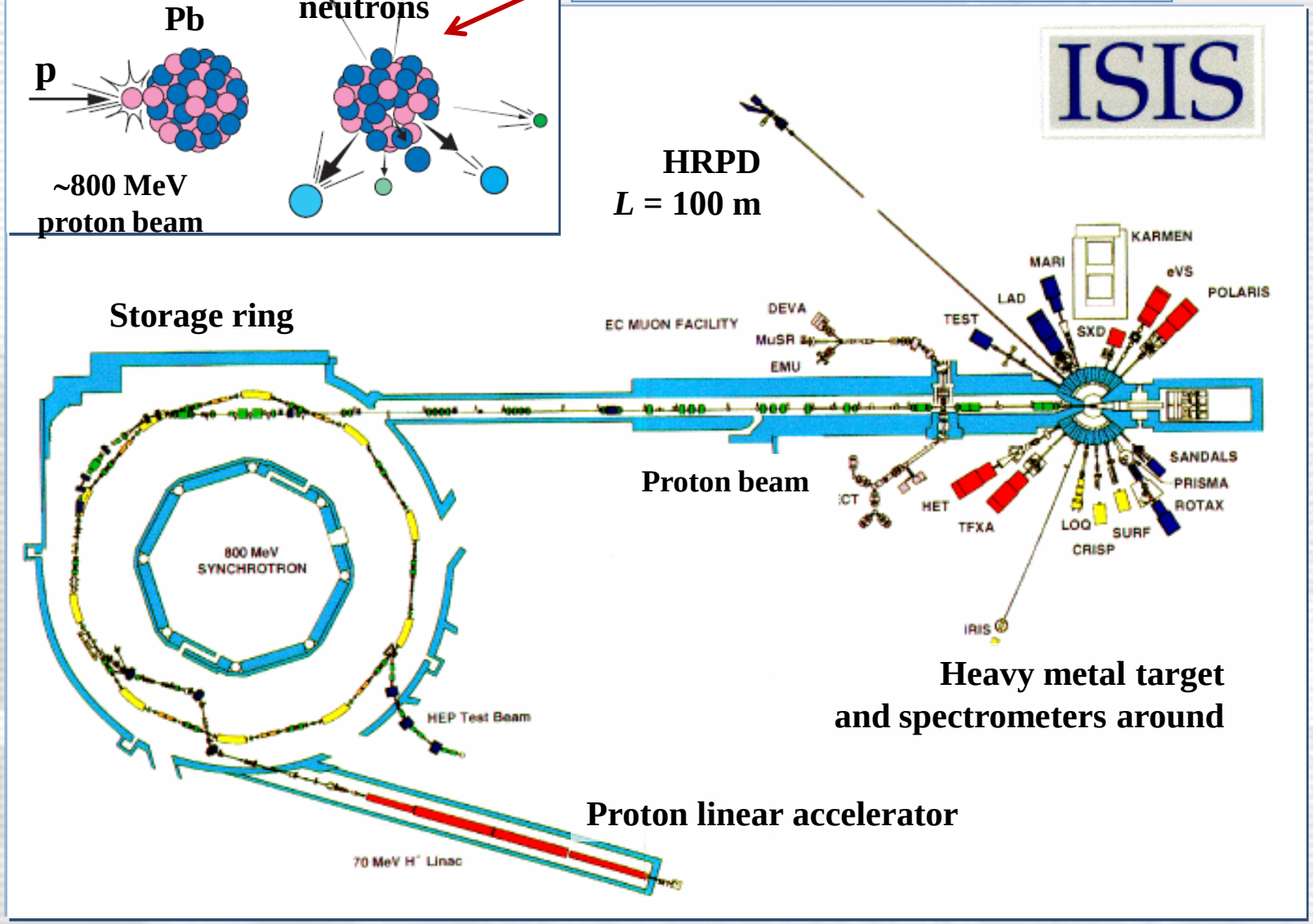

ISIS Neutron and Muon Source at the Rutherford Appleton Laboratory in Oxfordshire, UK

ISIS, UK
LANSCE, USA
SNS, USA
JSNS, Japan
CSNS, China
IBR-2, Russia
ESS, Sweden

Only 6 now

Special features of neutron diffractometers

Steady state source

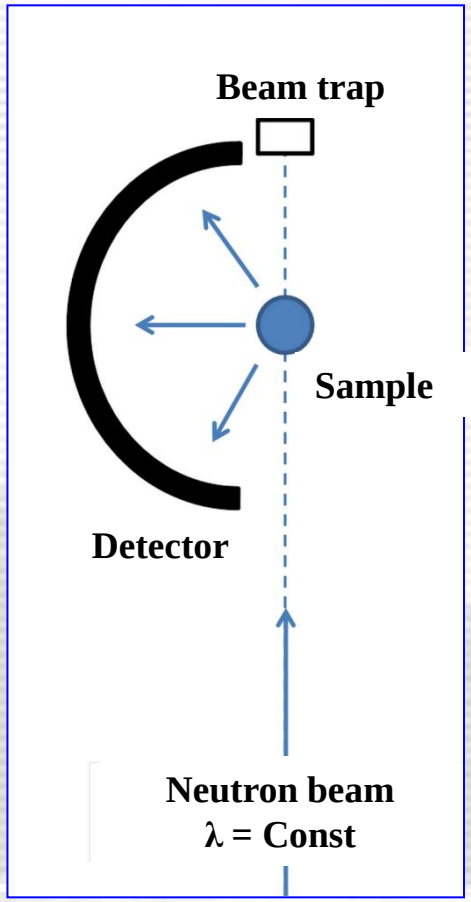

$\lambda = \lambda_0$, $\theta_1 \leq \theta \leq \theta_2$

λ = const diffractometer

I. Experiment with single crystal
2D PSD, (Δx, Δy) < 3x3 mm

II. Atomic structure (powder)
$\Delta d/d \approx 0.002$, wide-aperture detector

III. Magnetic structure (powder)
$\Delta d/d \approx 0.02$, large (~15 Å) d_{hkl}

IV. *In situ, real-time* experiment
high flux, wide range of d_{hkl}

V. High pressure, micro samples
high flux, low background

VI. Macromolecular structures
$\Delta d/d \approx 0.02$, large (~60 Å) d_{hkl}

VII. Local structural distortions
large Q_{max} (> 40 Å^{-1})

VIII. Microstructure of materials
$\Delta d/d \approx 0.004$, high flux

Pulsed source

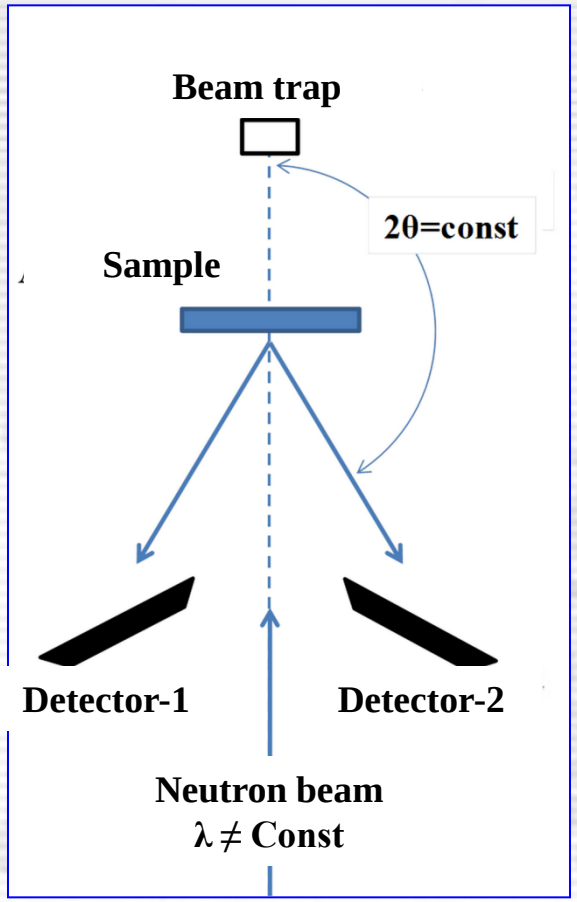

$\theta = \theta_0$, $\lambda_1 \leq \lambda \leq \lambda_2$

TOF diffractometer

Complementarity of λ = const и TOF-diffractometers

Structural experiment

λ = const diffractometer

TOF diffractometer

Experimental data are obtained with different weights for different points in reciprocal space

A routine experiment can be carried out with equal success on both types of diffractometers

A non-standard (precision) experiment requires an adequate choice of the type of diffractometer

A sophisticated experiment often requires performing it on both types of diffractometers

Standard powder $Na_2Al_2Ca_3F_{14}$

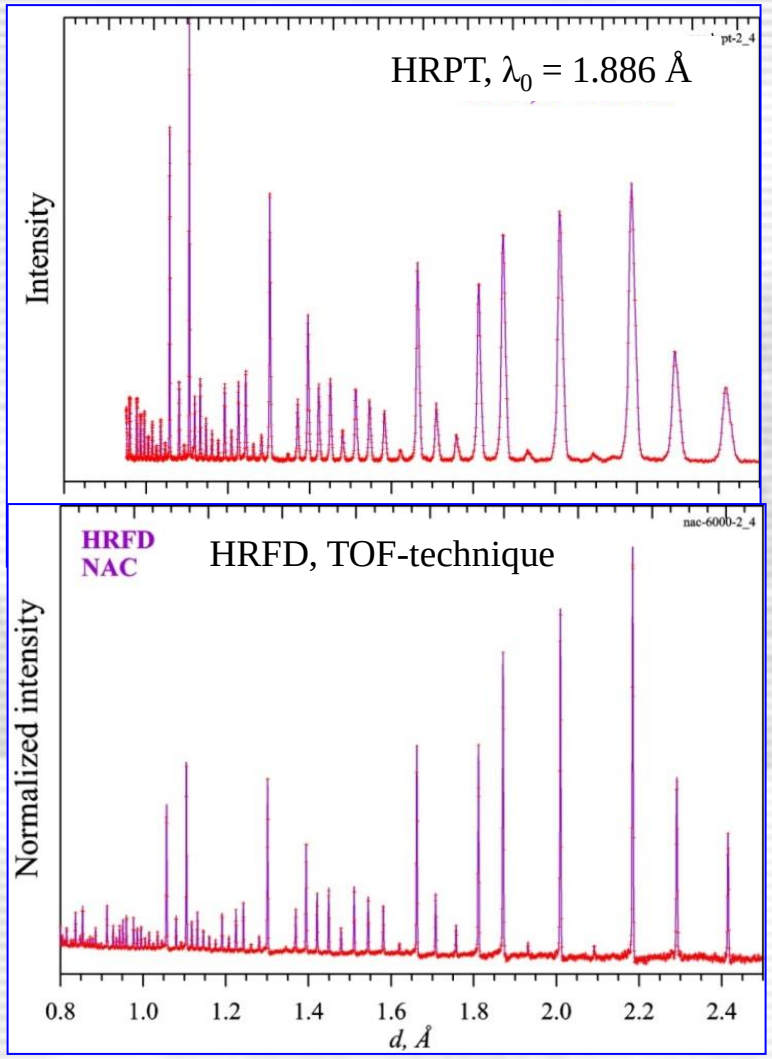

Spectrometers' at the IBR-2 pulsed reactor

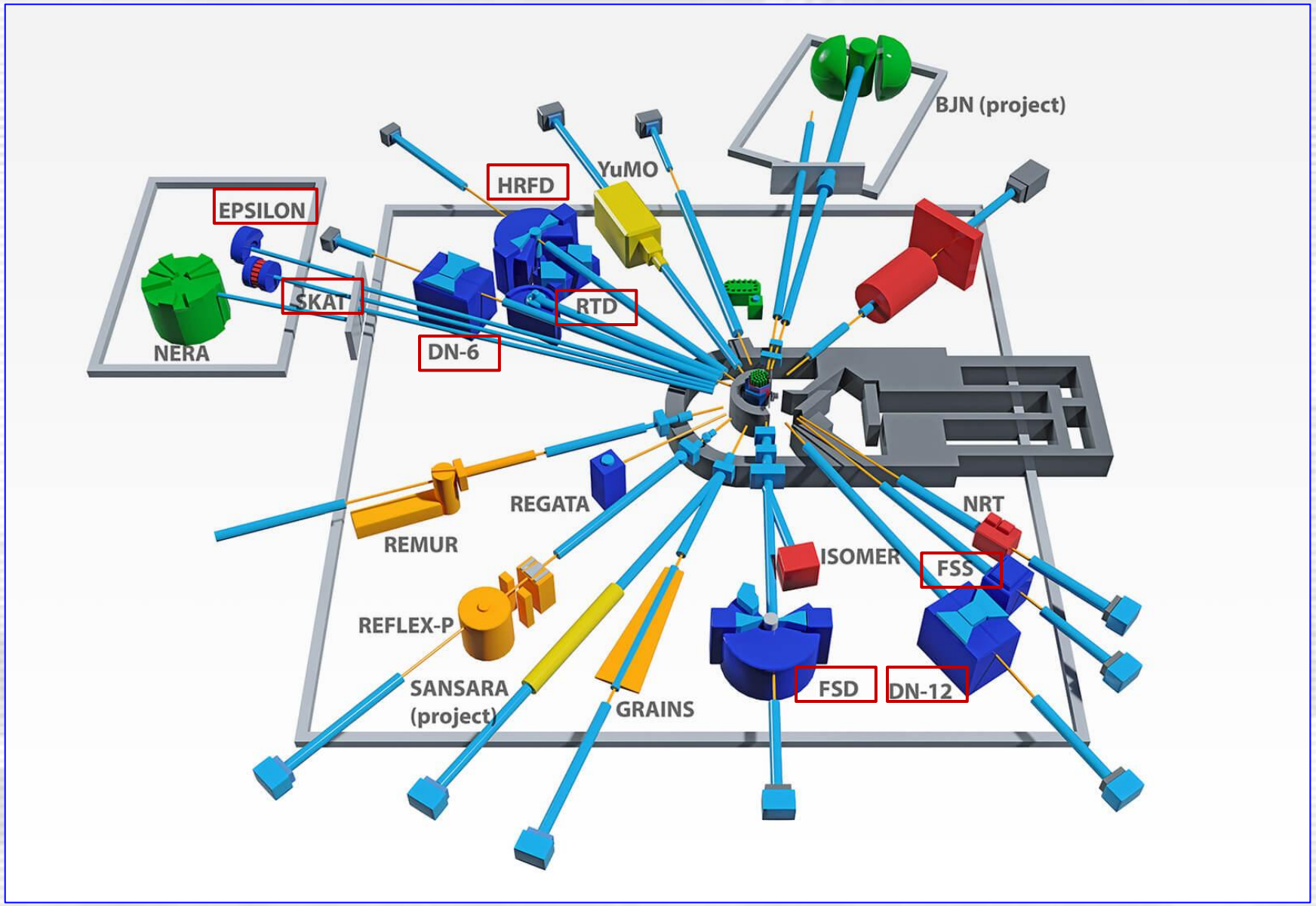

Operational:

- Diffraction: 8
- SANS: 1
- Reflectometry: 3
- Inelastic: 1
- Imaging: 1

Projects:

- BJN (inelastic)
- Sansara (SANS)

Diffraction at IBR-2

1.	HRFD*	powders – atomic and magnetic structure
2.	RTD (DN-2)	powders, single crystals – real-time, *in situ*
3.	DN-6	microsamples – high-pressure
4.	Epsilon**	rocks, bulk samples – internal stresses
5.	SKAT**	rocks, bulk samples – textures
6.	FSD*	bulk samples – material science
7.	DN-12	microsamples – high-pressure
8.	FSS*	bulk samples – internal stresses

* Fourier RTOF technique – a special feature of diffraction at the IBR-2 reactor

** Long (~100 m) flight pass

High Resolution Fourier Diffractometer. Collaboration: FLNP (Dubna) - PNPI (Gatchina) - VTT (Espoo)

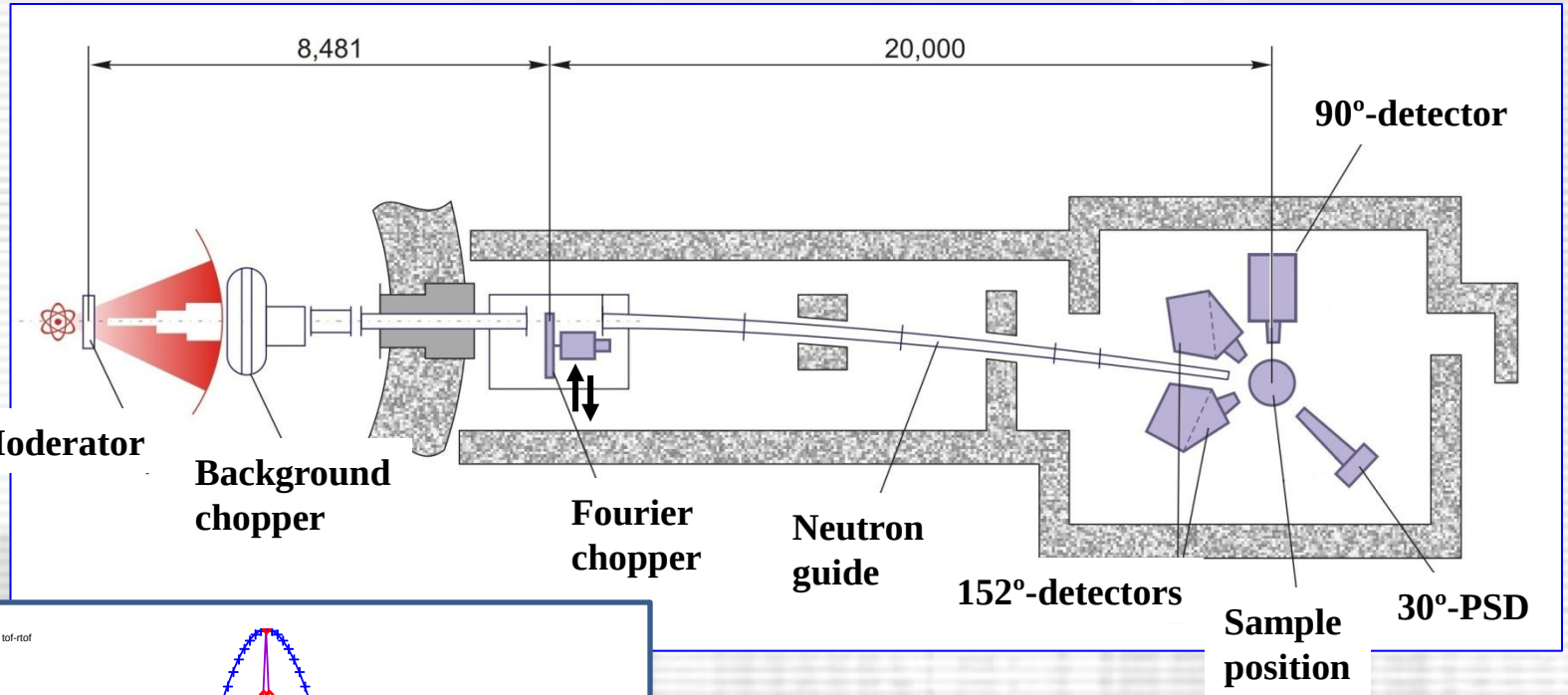

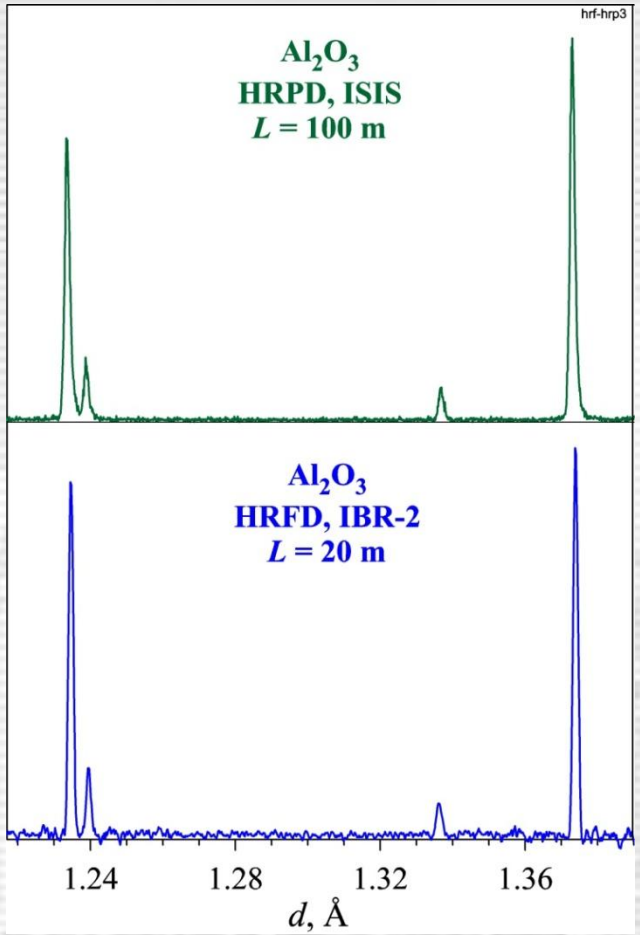

Diffraction patterns of Al_2O_3 measured at HRPD (L = 100 m, ISIS, UK) and HRFD (L = 20 m, IBR-2, Dubna).

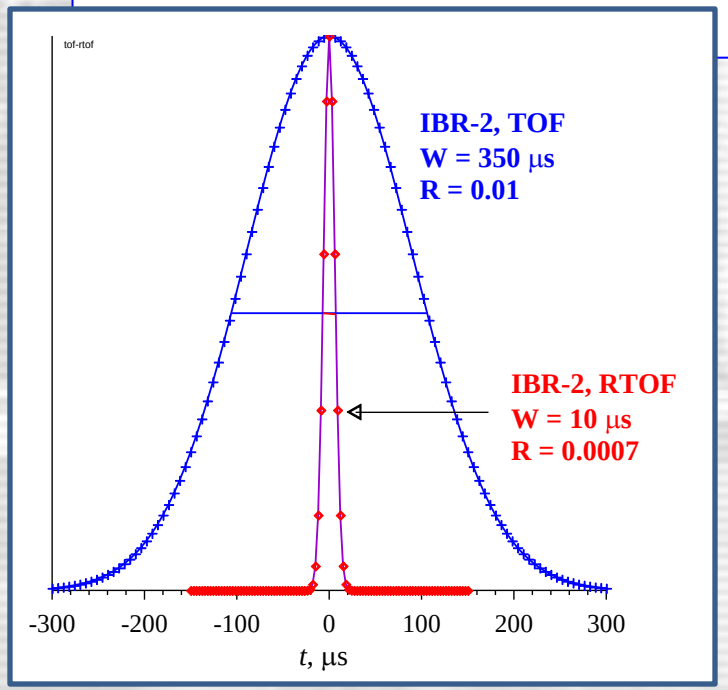

HRFD at the IBR-2 pulsed reactor: A new concept / A.M. Balagurov et al., NIM (2018)

Fast Fourier chopper at HRFD (Dubna)

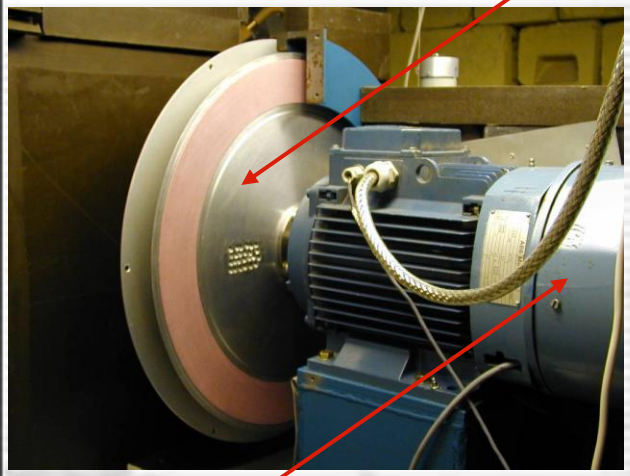

7.5 kW motor

Rotor (∅ = 50 cm)

0.7 mm

Stator

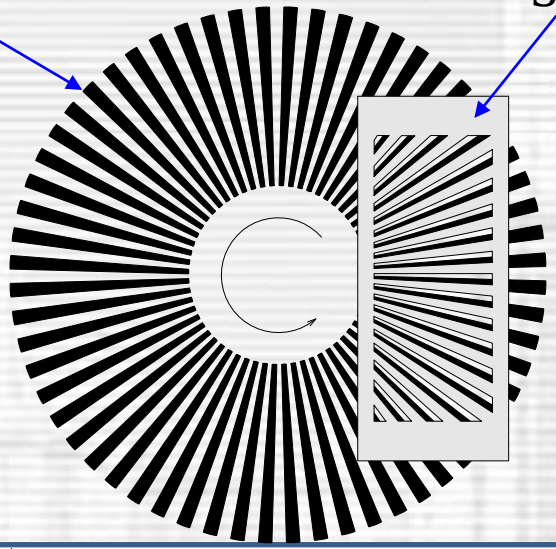

Sample position, about 30 m from moderator.

Triangular chopper transmission function:

$T(t) \approx 1 + \sin \omega t$

Binary pick-up signals for RTOF analyzer

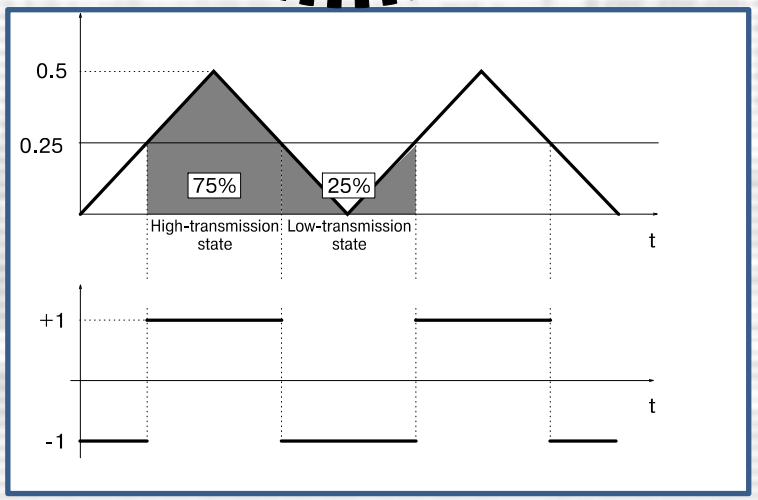

Comparison of diffraction patterns of Y-123 HTSP, mesured with high- and medium-resolution

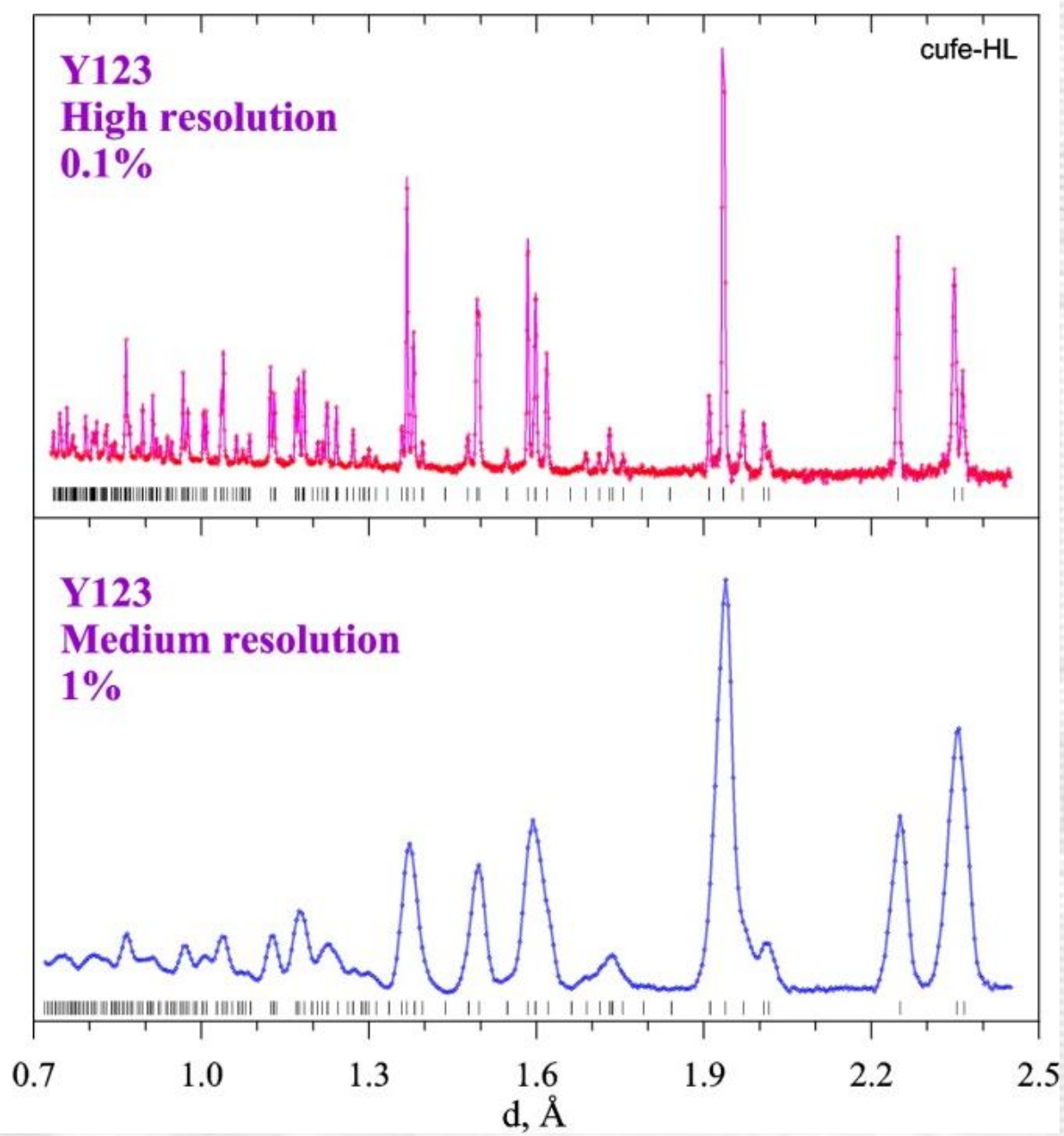

Measured on the $La^{11}B_6$ powder HRFD resolution function at chopper rotation frequencies of 2500, 4000 and 6000 rpm

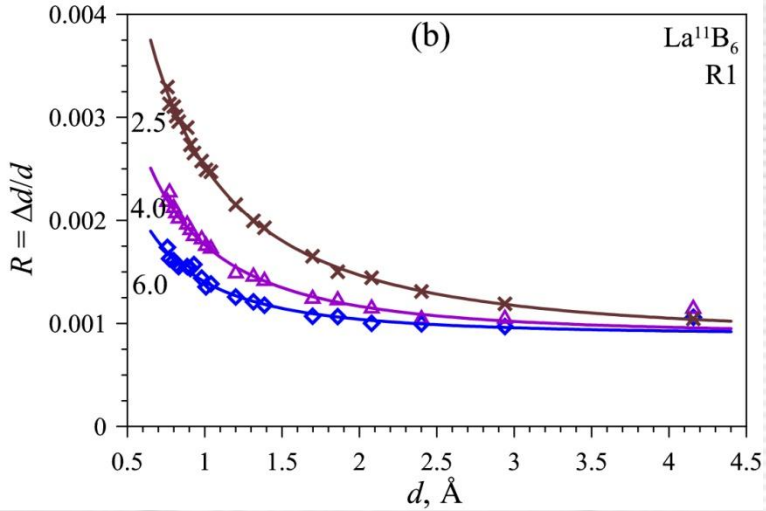

α-SiO_2 single crystal diffraction pattern for [*hh*0] line

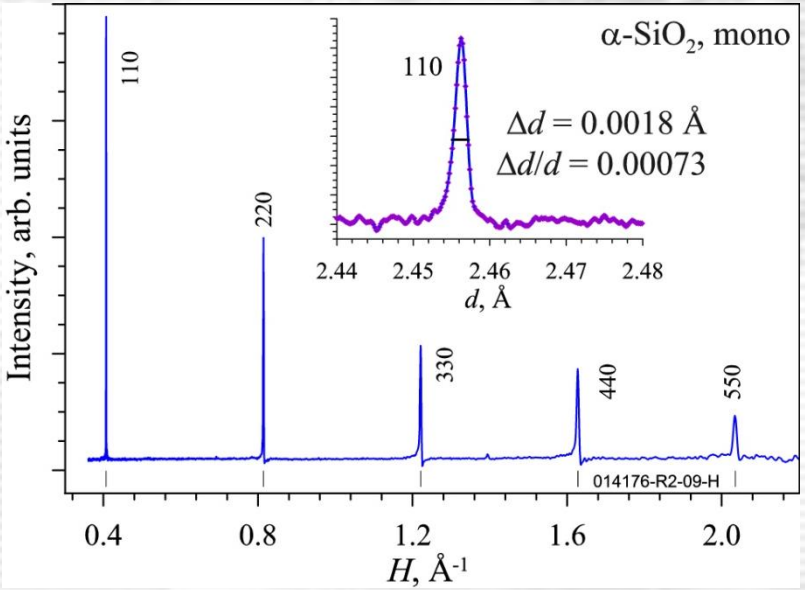

Mercury based HTSC (MSU + FLNP): $HgBa_2CuO_{4+\delta}$

Crystal structure of Hg-1201

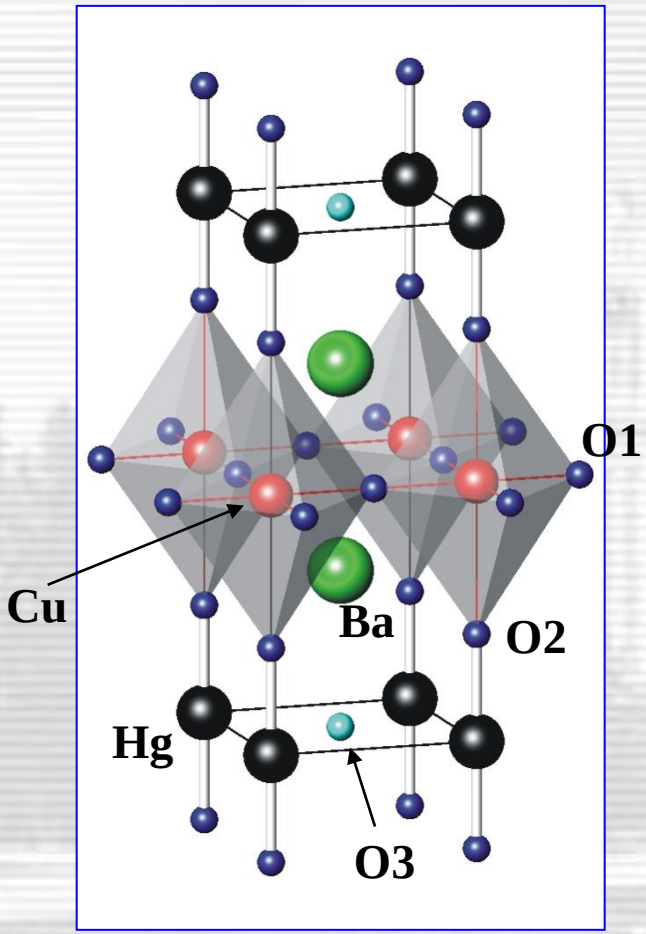

In Hg-1201 O3 position is filled partly: n(O3) = δ = 0.12

Rietveld refinement of $HgBa_2CuO_{4.12}$ structure

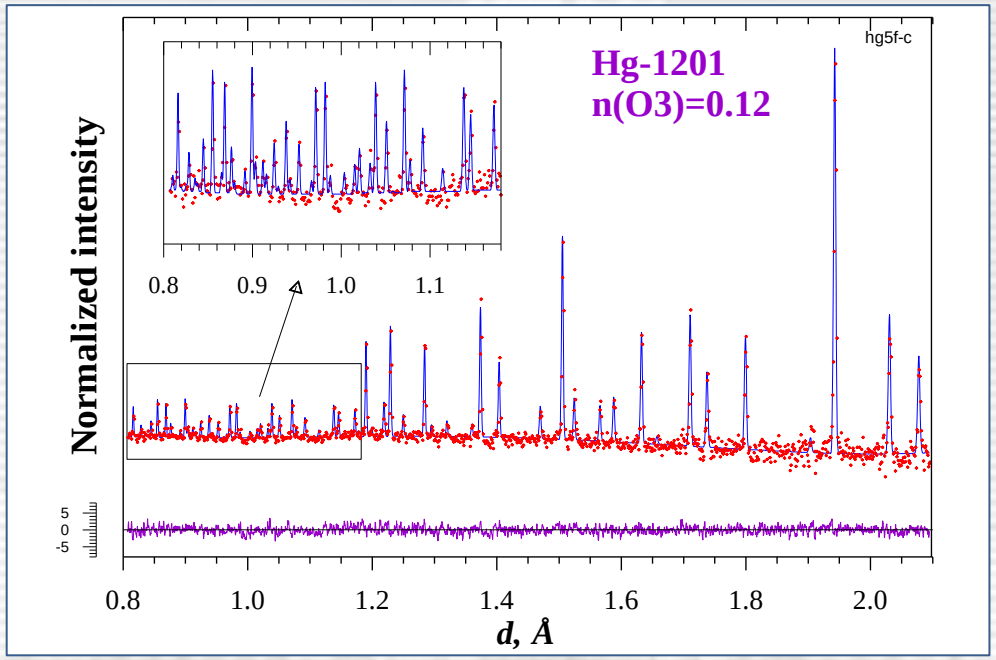

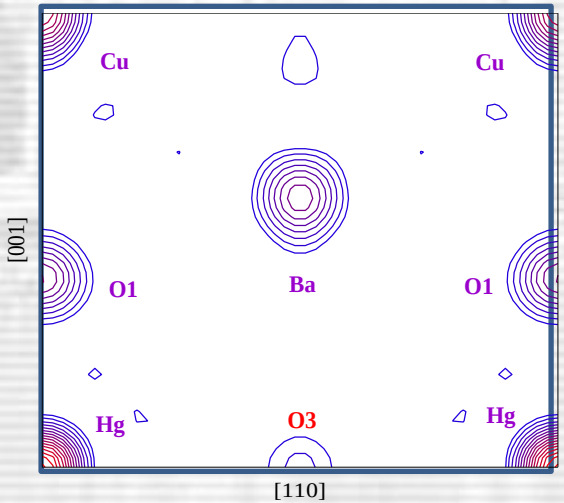

Oxygen vs. fluorine content

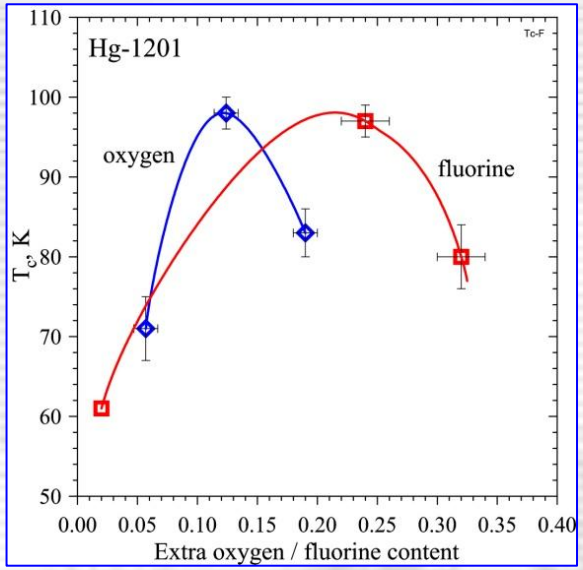

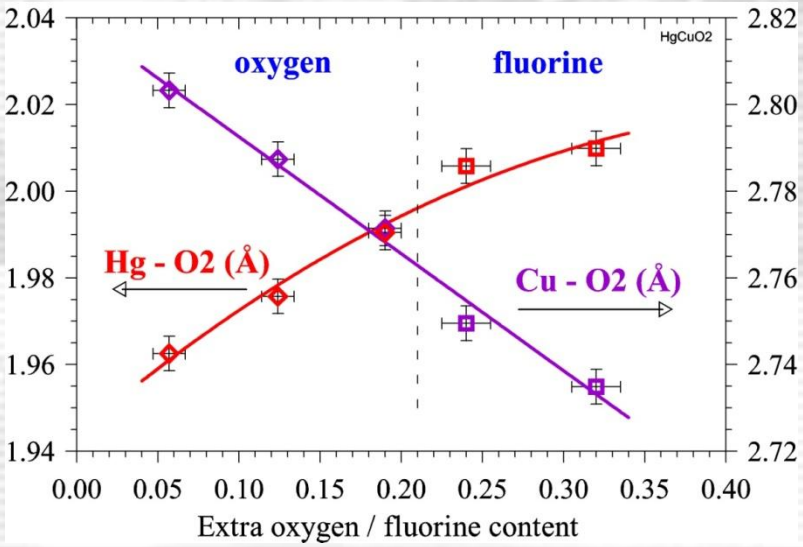

Structural and magnetic (spin-flip) phase transitions in Fe_3Ge alloy

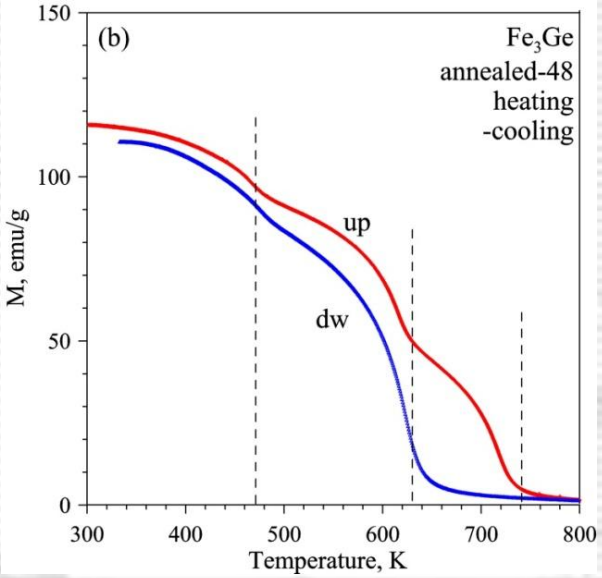

Temperature dependencies of the specific magnetization during heating (up) and cooling (dw) for the annealed-48 sample.

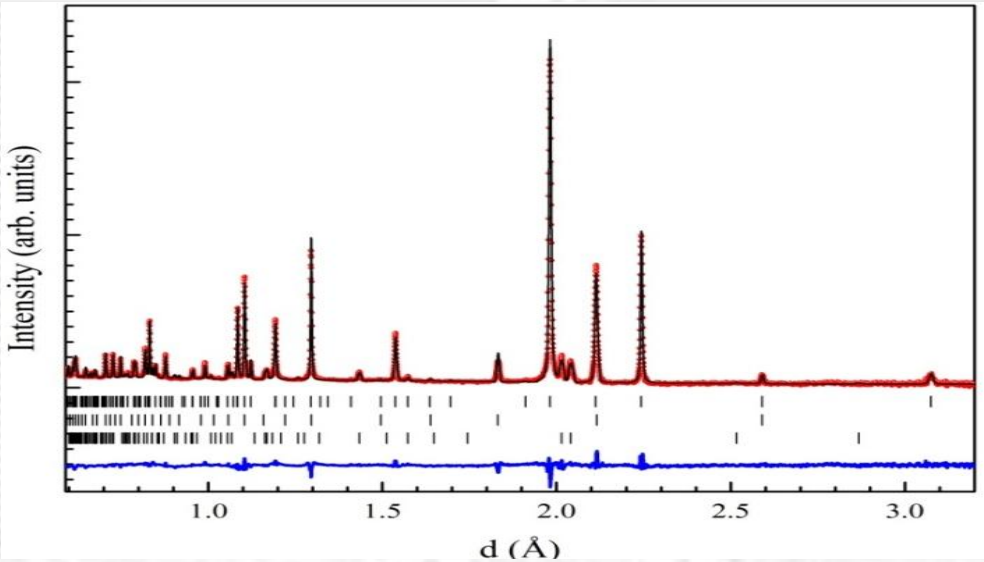

Neutron diffraction pattern (high resolution) of annealed-24 Fe_3Ge sample collected at RT and processed by the Rietveld method. The vertical bars are calculated peak positions of the $D0_{19}$, $L1_2$, and $B8_2$ phases (from top to bottom).

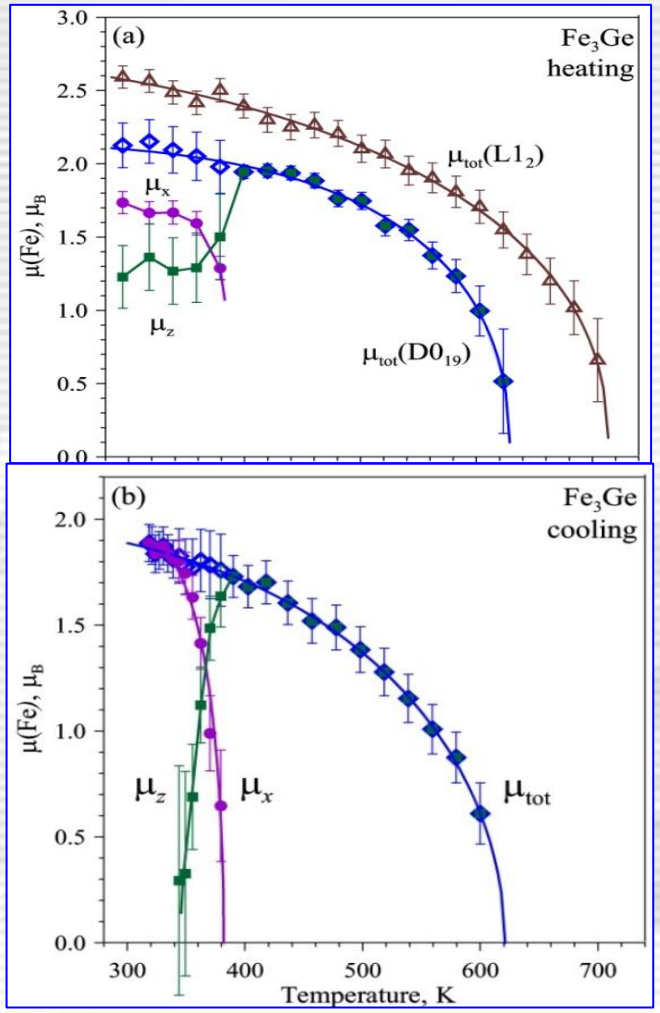

Magnetic moments of the $D0_{19}$&$L1_2$ at heating and the $D0_{19}$ phases at cooling. The components in basal plane (μ_x) and along hexagonal axis (μ_z) are shown.

Single crystal diffraction at RTD

2D PSD, (Δx, Δy) < 3 x 3 mm, $\Delta d/d \approx 0.02$

Advantages of neutron diffraction

- Light elements: H, Li, C, O
- Isotope contrasting: H → D
- Negative scattering density
- Strong magnetic interaction
- 2D & 3D scanning of RS
- High penetration depth
- Large beam cross-section

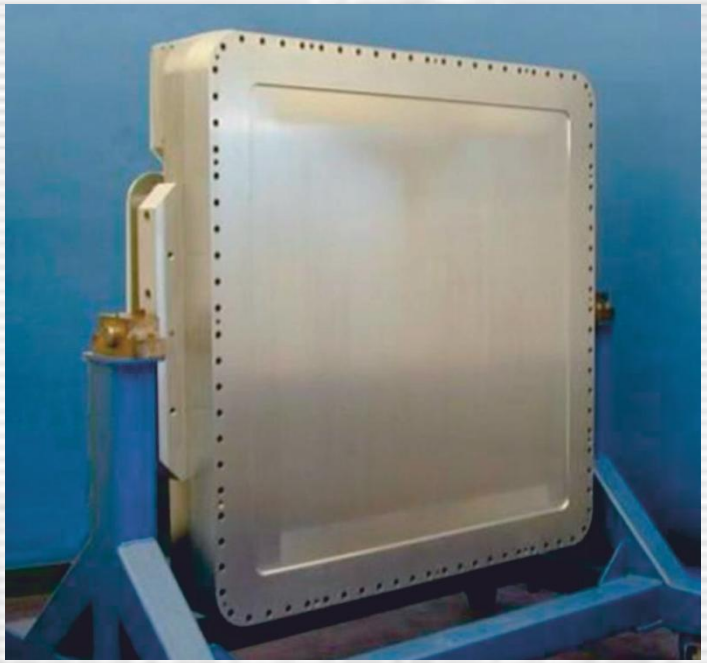

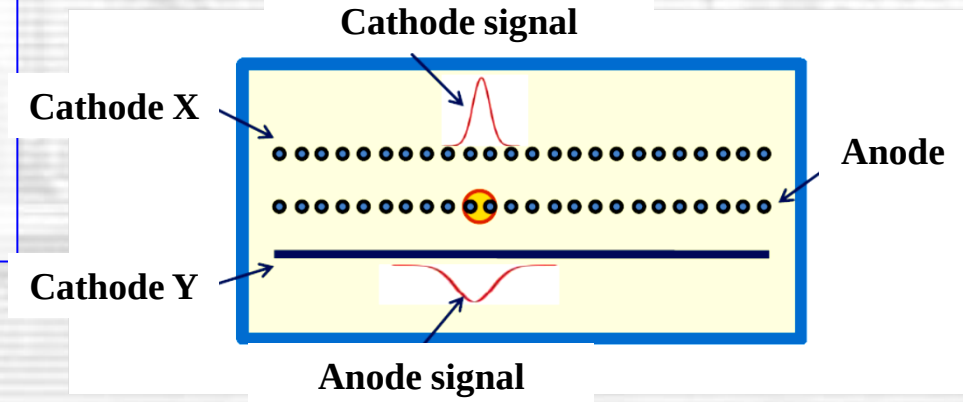

2D PSD, (Δx, Δy) < 3 x 3 mm

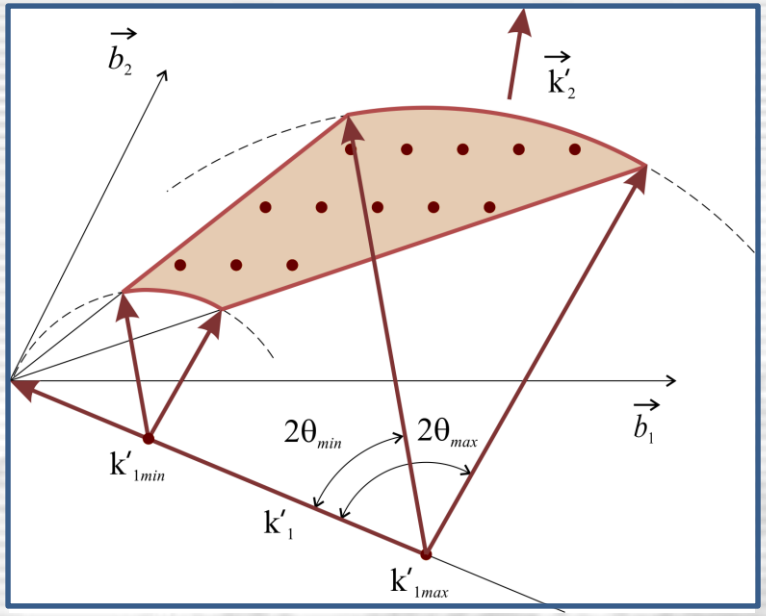

TOF-diffractometer with 1D PSD.
The *k*-vector range is (k'_{min}, k'_{max}), the scattering angle range ($2\theta_{min}$, $2\theta_{max}$) is covered by position sensitive detector.

2D: $\theta_1 \le \theta \le \theta_2$
$\lambda_1 \le \lambda \le \lambda_2$

3D: $\theta_1 \le \theta \le \theta_2$
$\varphi_1 \le \varphi \le \varphi_2$
$\lambda_1 \le \lambda \le \lambda_2$

Multidimensional neutron single crystal diffractometry

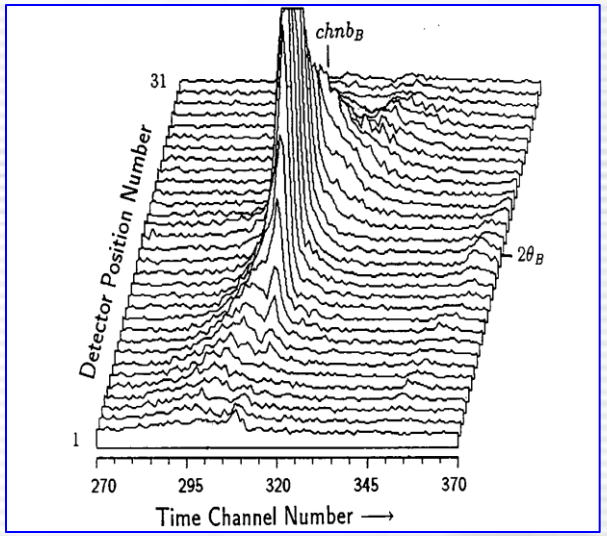

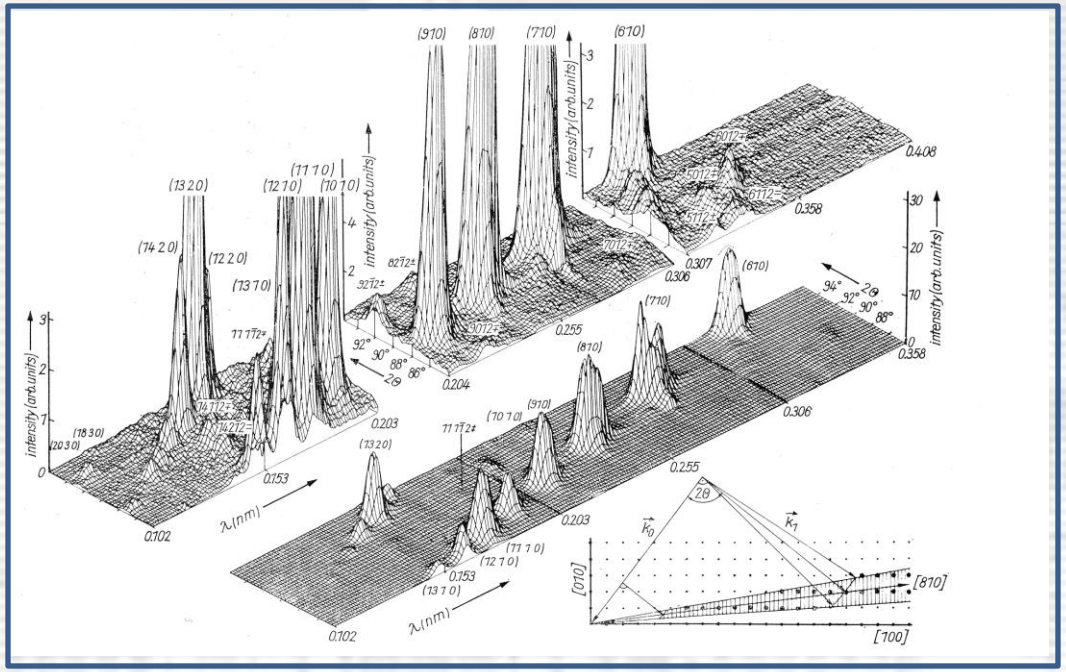

[801] measured sector in incommensurate phase of $Sr_{0.7}Ba_{0.3}Nb_2O_6$

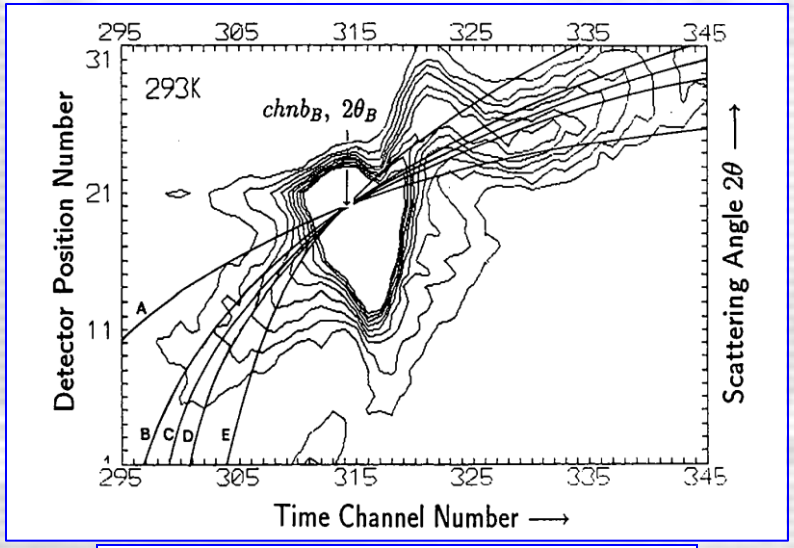

Diffuse scattering in the $Sr_{0.7}Ba_{0.3}Nb_2O_6$ crystal

Diffraction line splitting in multi-domain state of KD_2PO_4. 1D PSD, up to $15 \cdot 10^3$ points can be measured simultaneously.

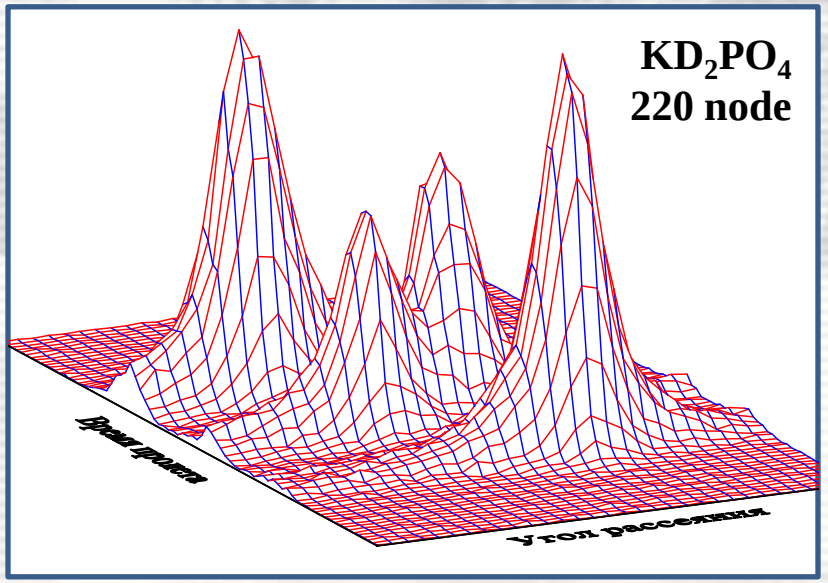

In situ – real-time studies of irreversible processes in crystals: $A \sim A_{\infty}[1 - \exp(-t/\tau)]$

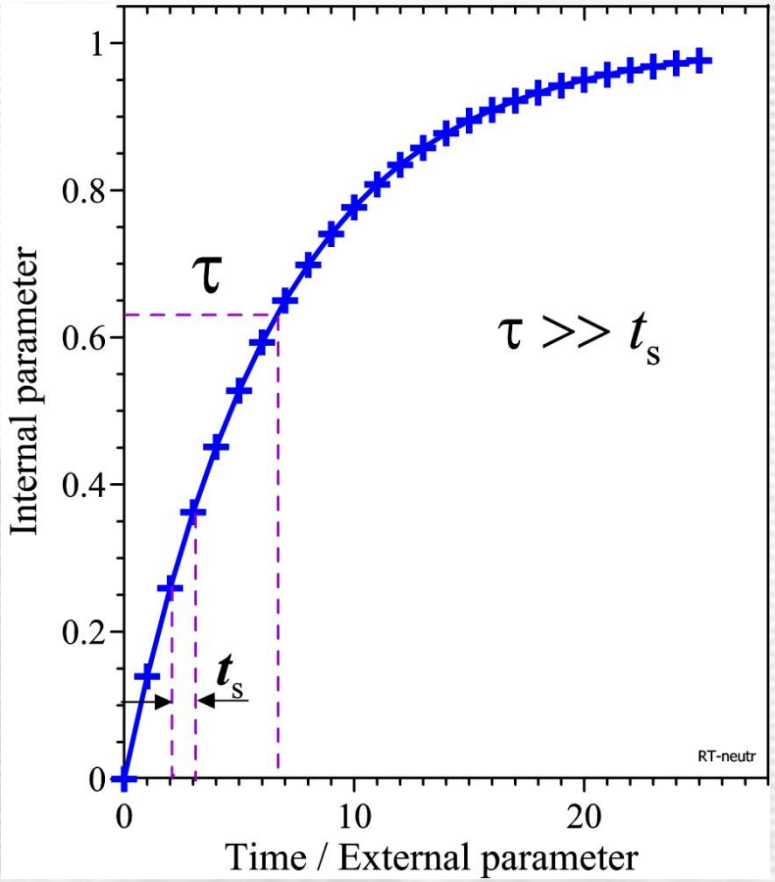

$\Delta t = t_s$ – temporal resolution

Processes:

1. Solid state chemical reaction
2. Isotope exchange
3. Structural phase transitions
4. Electrochemical processes
5. Swelling

Main condition:

$t_s << \tau$,

например, $t_s = \tau/10$

$\tau \sim 10$ s – 1 hour

$t_s \approx 1$ s – 10 min

Diffractometers:

Steady state reactors:

ILL (Grenoble)	D20	$t_s \sim 1$ s – 5 m
PSI (Swiss)	HRPT	$t_s \sim 1$ – 5 m

Pulsed neutron sources:

ISIS (UK)	Polaris	$t_s \sim 5$ m
	GEM	$t_s \sim 1$ - 5 m
SNS (USA)	VULCAN	$t_s \sim 0.5$ – 5 m
LANSCE (USA)	HIPD	$t_s \sim 1$ - 5 m
J-PARC (Japan)	HITD	$t_s \sim 1$ – 5 m
IBR-2 (Russia)	HRFD	$t_s \sim 10$ s – 1 m
ESS (Sweden)	SPD	$t_s \sim 0.3$ ms – 0.5 s

Formation of $YBa_2Cu_3O_x$ through a solid-state reaction of Y_2O_3, $BaCO_3$ and CuO in air

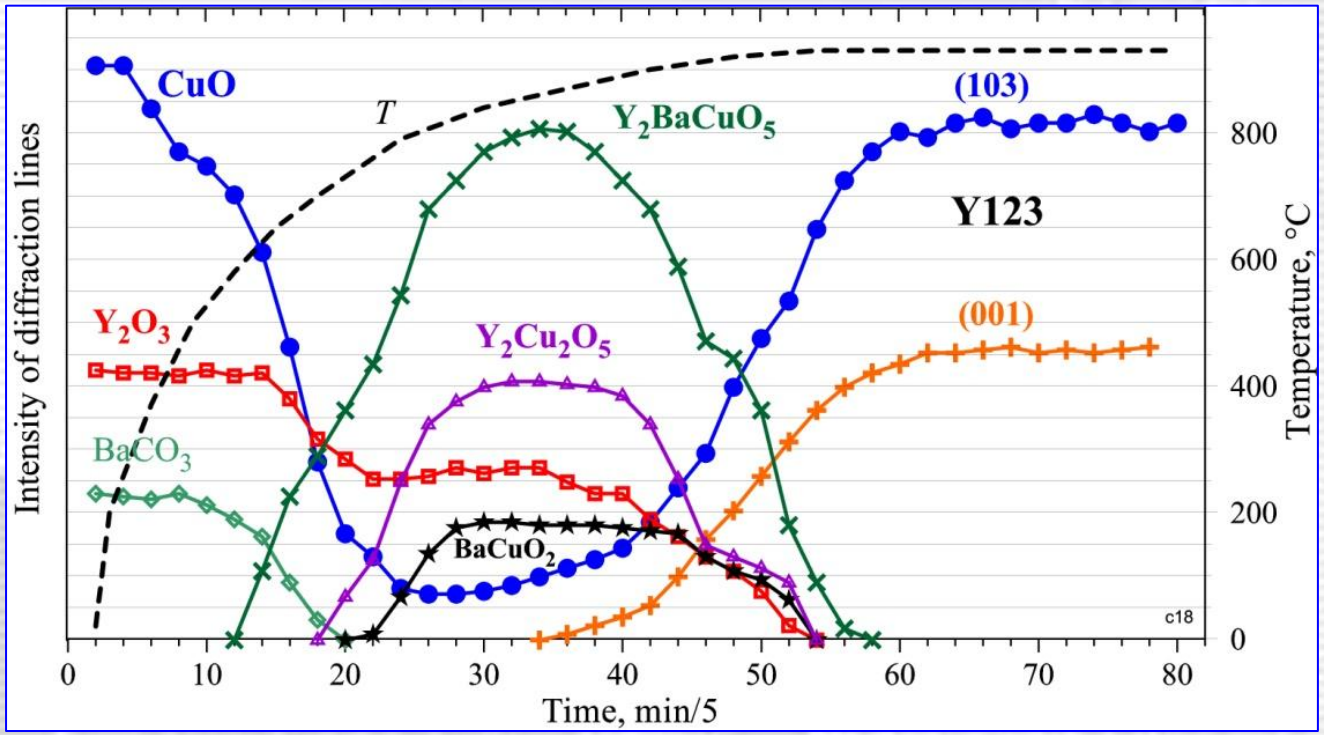

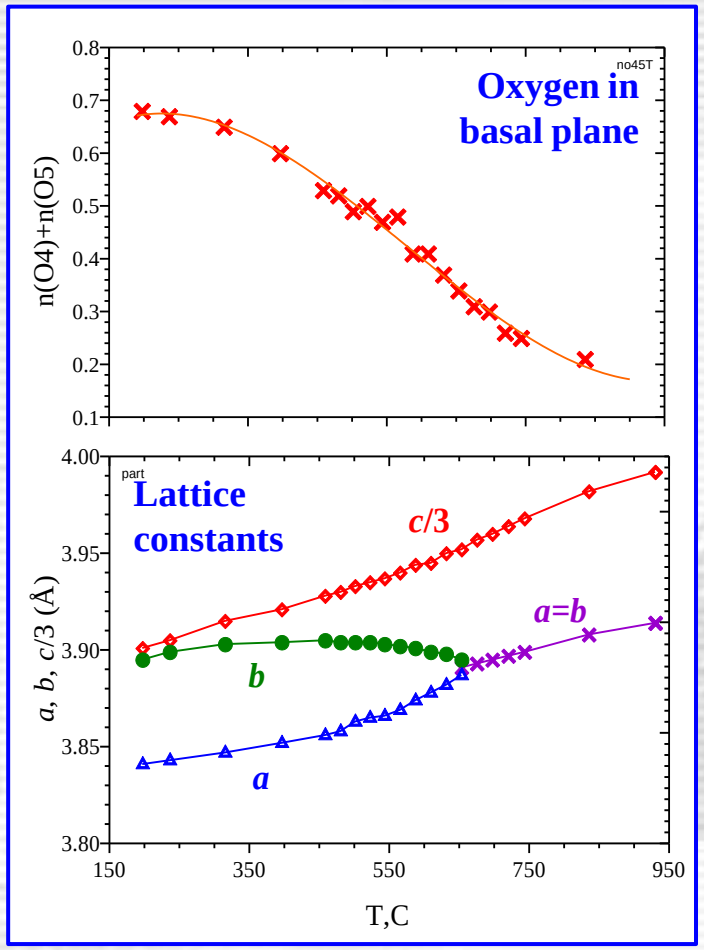

$\{Y_2O_3 + BaCO_3 + CuO\} \Rightarrow$

$\Rightarrow \{Y_2BaCuO_5 + Y_2Cu_2O_5 + BaCuO_2\} \Rightarrow$

$\Rightarrow YBa_2Cu_3O_x$

$20°C \leq T \leq 940°C, \quad t_s = 5$ min

Cooling from 950°C down to RT.

***P4/mmm* ⇒ *Pmmm* transition**

$H_2O \leftrightarrow D_2O$ exchange in dipalmitoylphosphatidylcholine (DPPC) multilayer lipid membrane (t_s = 2 sec) (exponential law)

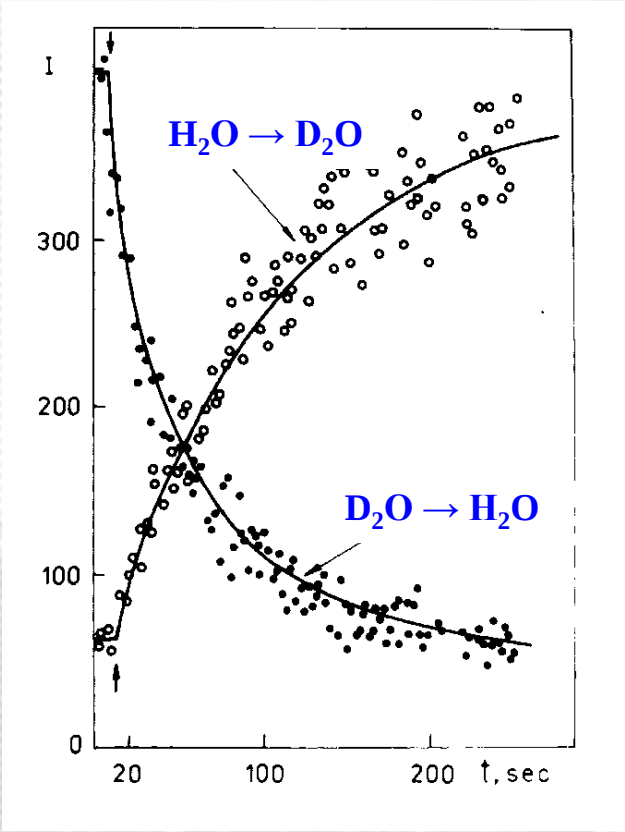

Intensity as a function of time

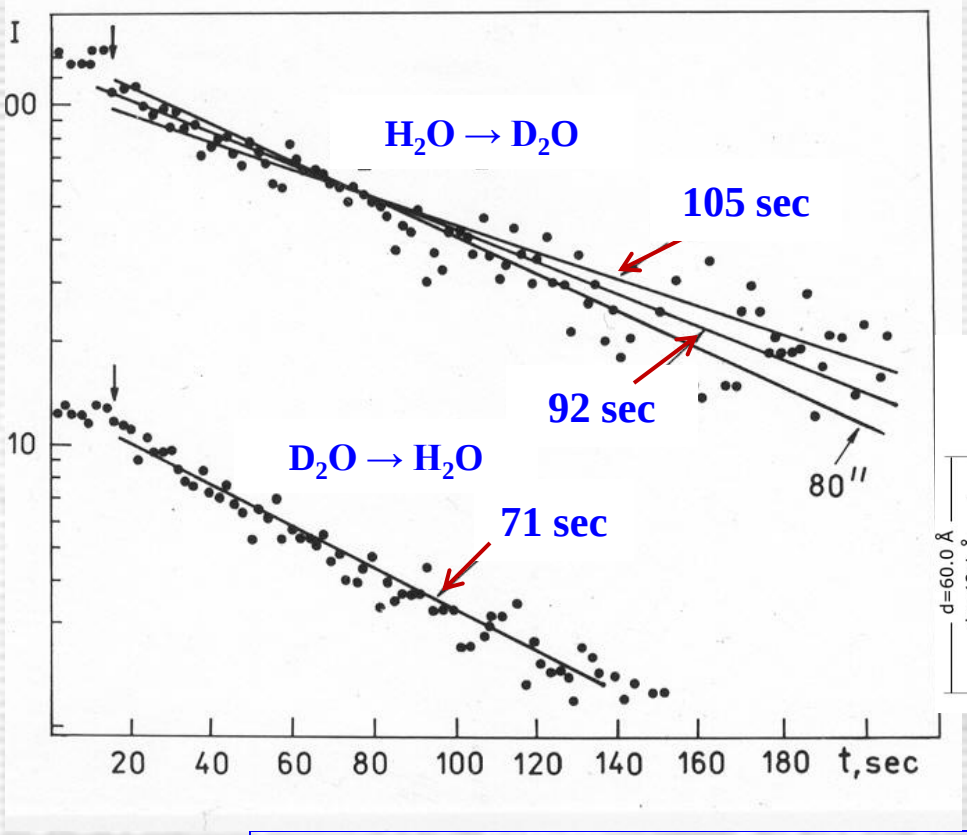

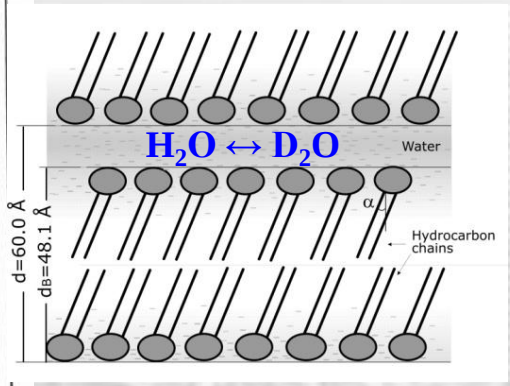

$F(t) = F_\infty + C \cdot e^{-t/\tau}$ or $F(t) = F_\infty \cdot (1 - C \cdot e^{-t/\tau})$

$\ln(F(t) - F_\infty) = \ln C - t/\tau$ → linear function

$y = \ln|F(t) - F_\infty|$ for $H_2O \rightarrow D_2O$ and $D_2O \rightarrow H_2O$. Characteristic times are equal to 92 s and 71 s, correspondingly.

Lithium-ion battery

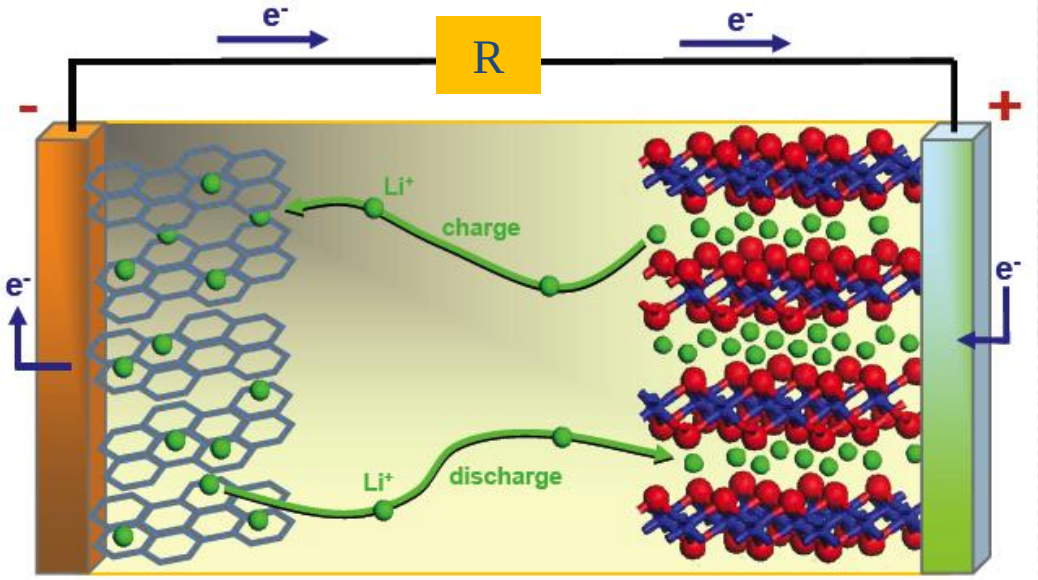

Li_xC_6 Organic electrolyte $LiMO_2$

$$C_6 + LiCoO_2 \underset{\text{discharge}}{\overset{\text{charge}}{\rightleftharpoons}} Li_xC_6 + Li_{1-x}CoO_2$$

$x \approx 0.5\text{-}0.6$

John B. Goodenough USA, 1922
Nobel Prize winner in 2019

K.Mizushima, P.Jones, P.Wiseman, J.B.Goodenough "Li_xCoO_2 (0<x<-1): A new cathode material for batteries of high energy density", 1980) 783–789

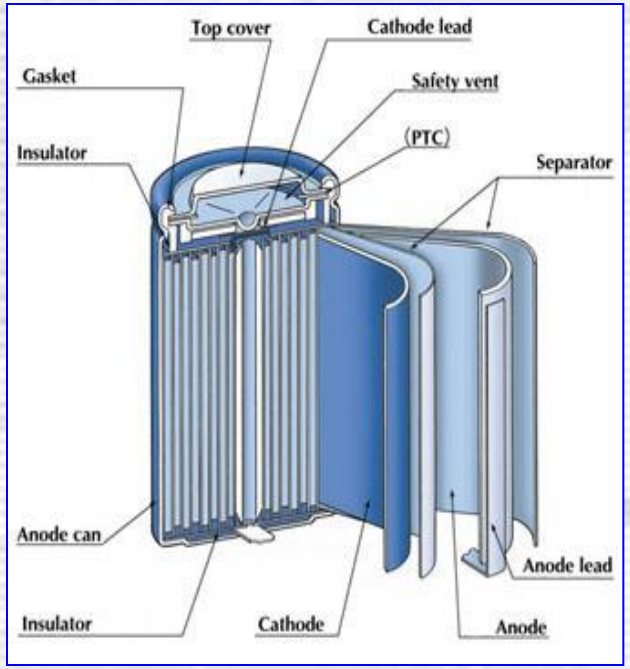

$LiFePO_4:V_\delta - Li_xC_6$ based battery, $\delta \approx 1\%$
Size = 8.2 x 128 x 155 mm

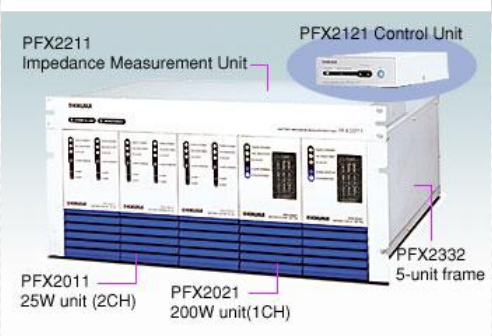

KIKUSUI PFX2011 potentiostat

$LiFePO_4:V_\delta$ – Li_xC_6 based battery. *In Situ* data (charge – discharge)

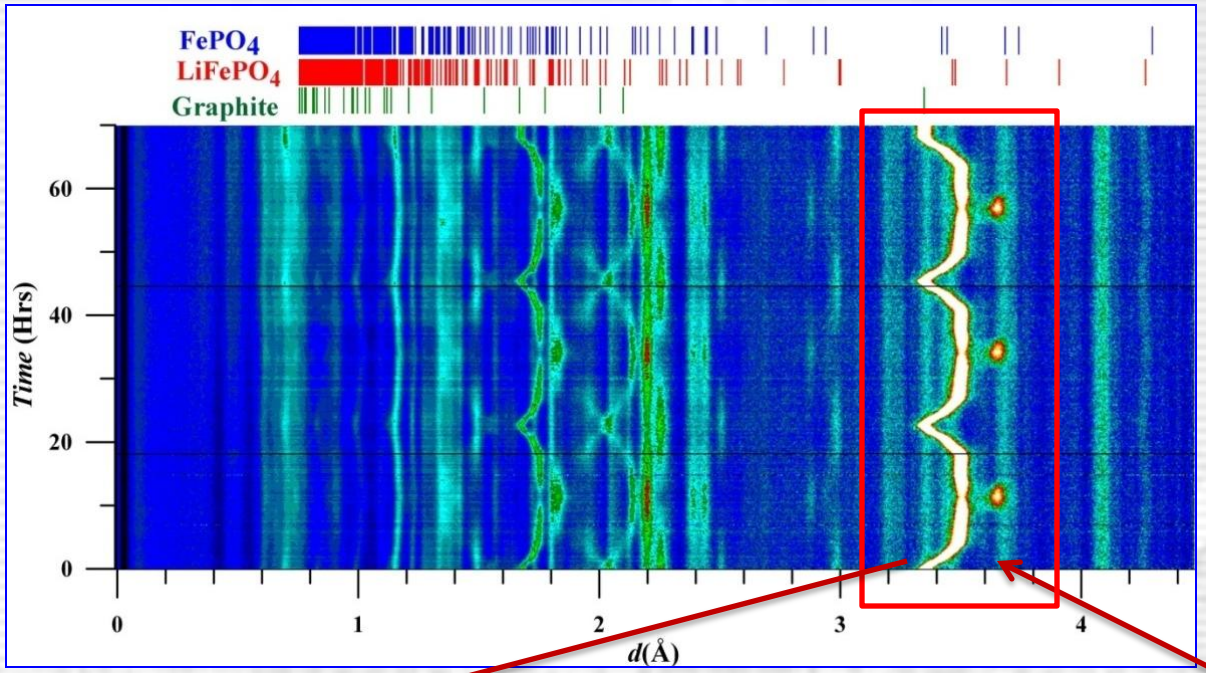

Evolution of the neutron diffraction patterns measured during three charge/discharge (~70 hours) cycles. "Anode window" is marked.

3D view of the "anode-window" region for all three cycles of charge/discharge processes

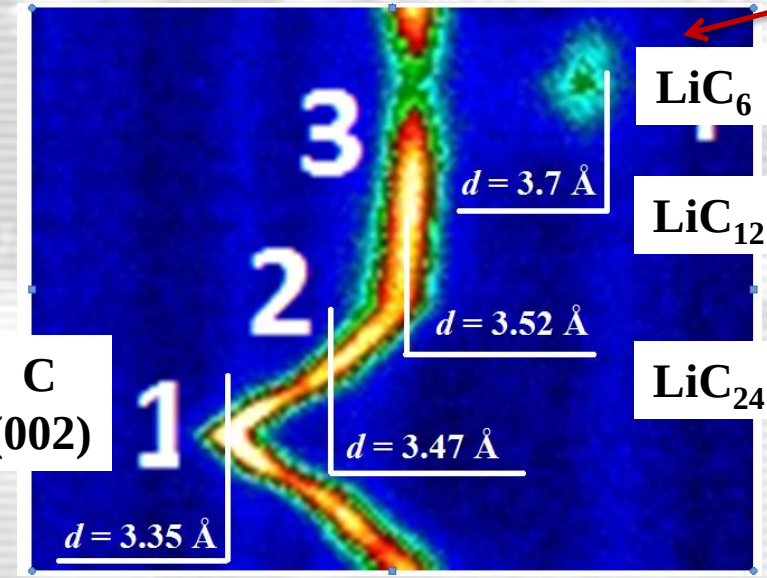

Enlarged chart of the initial (discharged) state with pure graphite line (d = 3.35 Å) and stepwise appearance of LiC_{24} (d = 3.47 Å) and LiC_{12} (d = 3.47 Å).

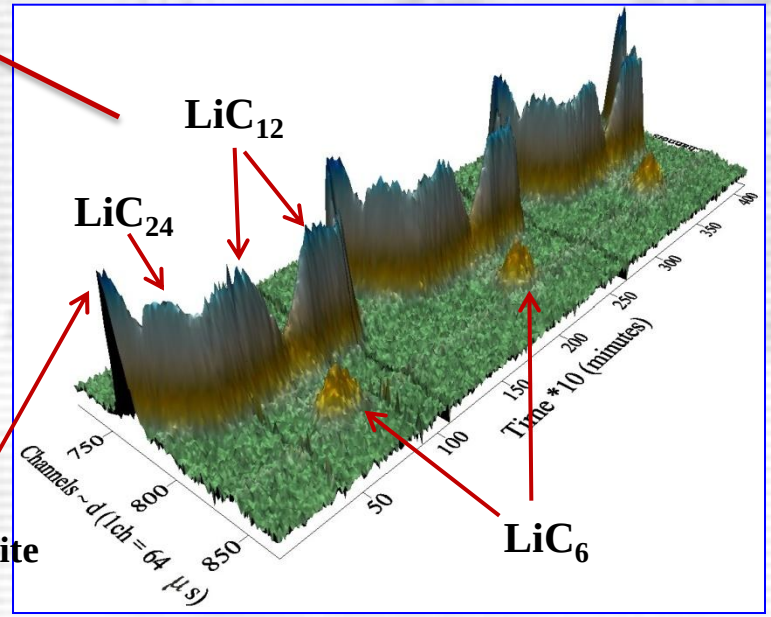

Fe-based alloys with giant (λ > 200 ppm) magnetostriction

Magnetostriction constant

	$\lambda = \Delta l/l$:
Fe	$\sim 20\times10^{-6}$
Fe-Al	$\sim 150\times10^{-6}$
Fe-19Ga	$\sim 400\times10^{-6}$

Galfenols: Fe-*x*Ga

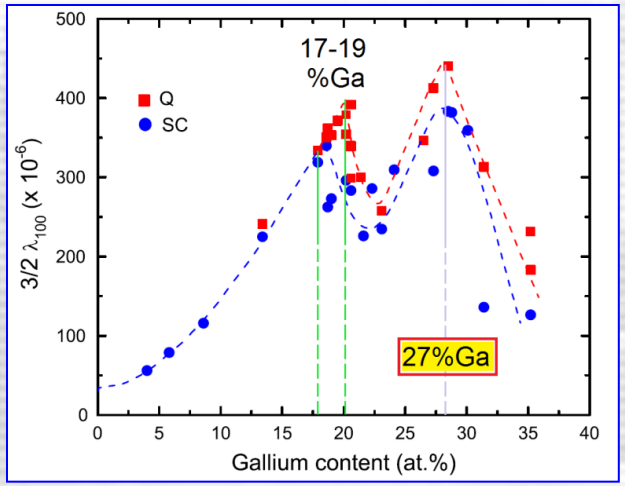

Local inhomogeneities

↓

high magnetostriction ?

Fe-27Ga: structural phases and neutron diffraction patterns

$D0_3$

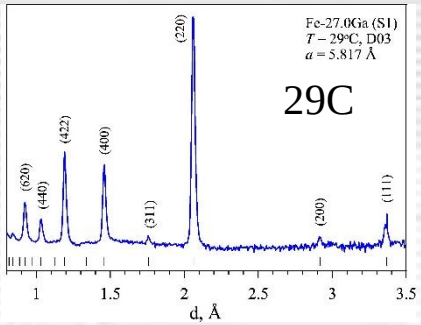

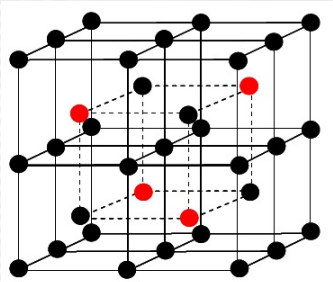

$L1_2$

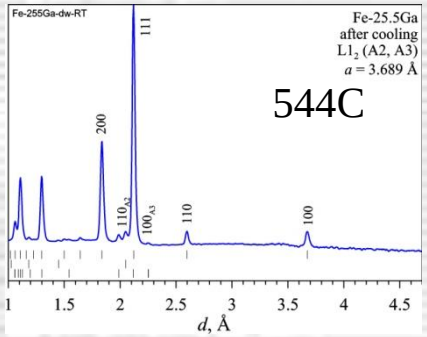

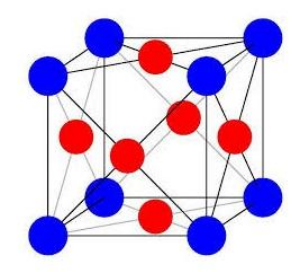

$D0_{19}$

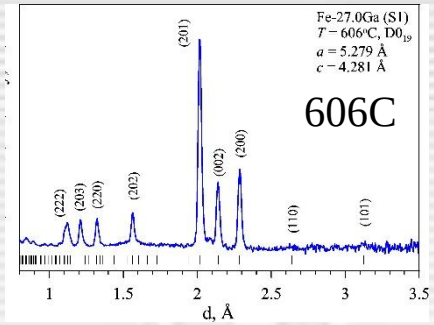

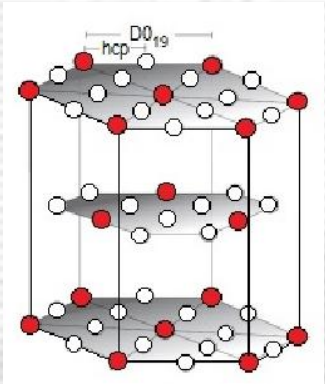

A2

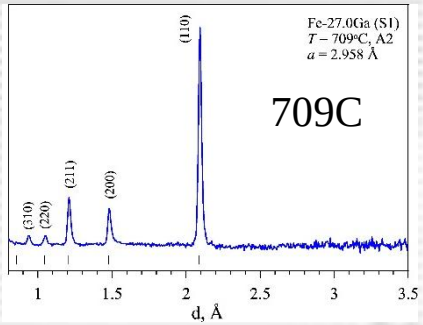

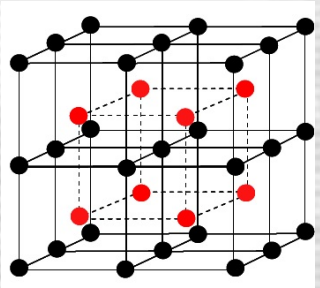

A2	α-Fe-type	atoms are randomly distributed	*Im3m*, $a \approx 2.92$ Å
B2	CsCl-type	atoms are partially ordered	*Pm3m*, $a \approx 2.92$ Å
$D0_3$	BiF_3-type	atoms are partially ordered	*Fm3m*, $a \approx 5.81$ Å
$L1_2$	Cu_3Au-type	atoms are partially ordered	*Pm3m*, $a \approx 3.72$ Å
$D0_{19}$	$MgCd_3$-type	atoms are partially ordered	$P6_3/mmc$, $a \approx 5.28$ Å, $c \approx 4.28$Å

$Fe_{73}Ga_{27}Dy_{0.5}$ alloy: structural transformations during heating – cooling process

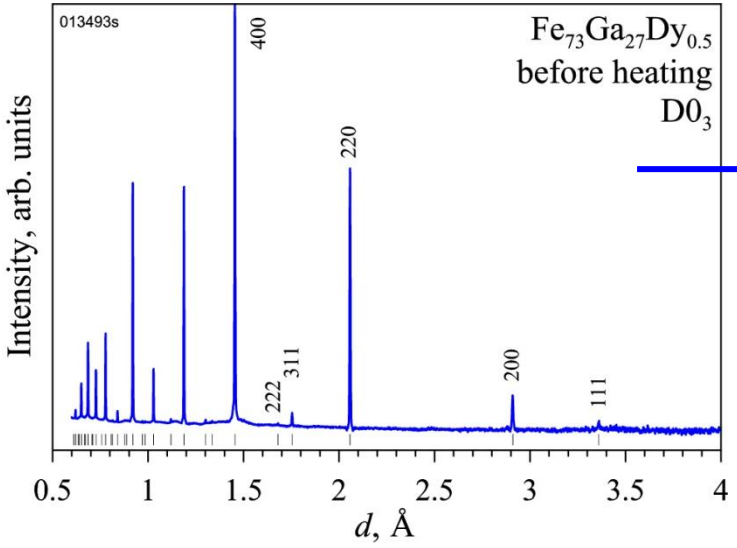

Before heating, $D0_3$ phase

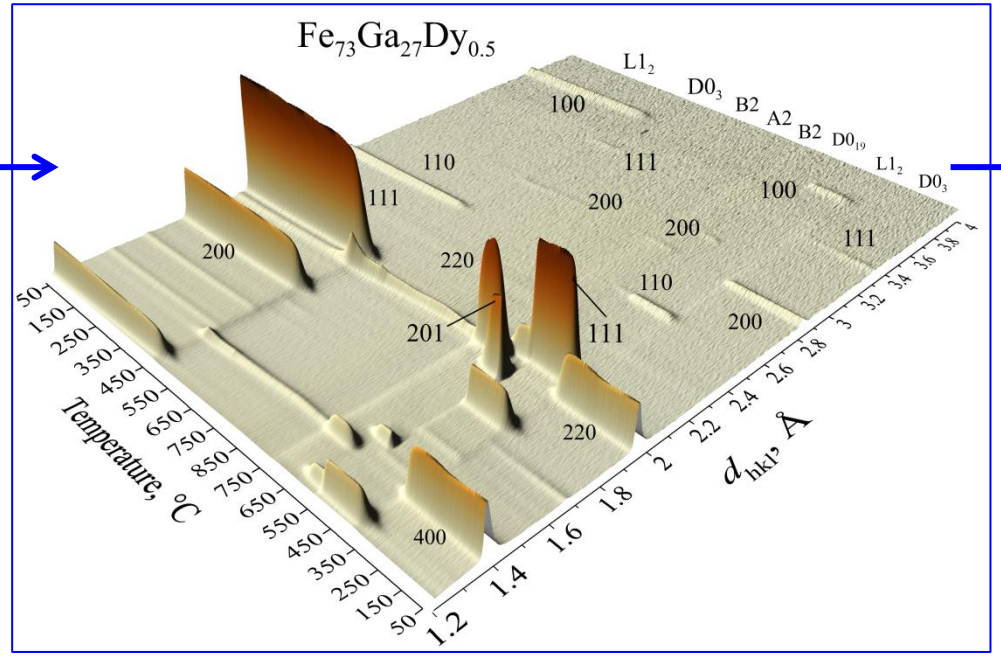

Heating up to 850°C, cooling down to 50°C

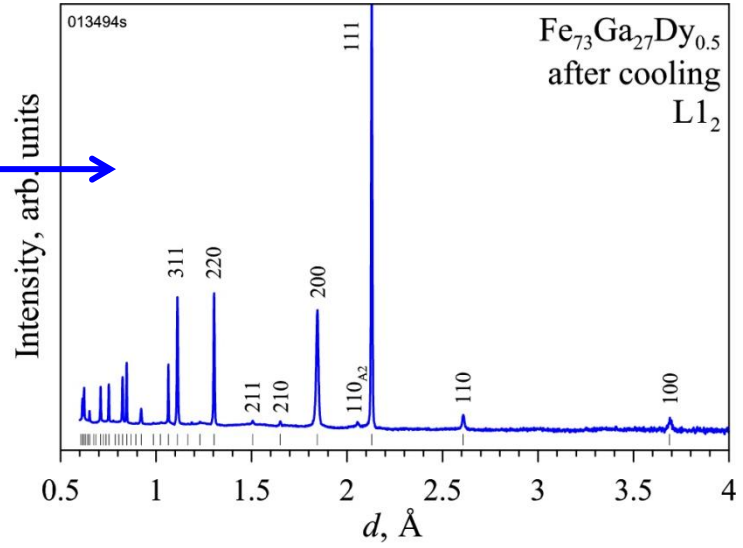

After cooling, $L1_2$ phase

<u>Temperature dependences of</u>:

- **Peak intensity → phase content,**
- **Peak position → atomic volume,**
- **Peak width → microstructure**

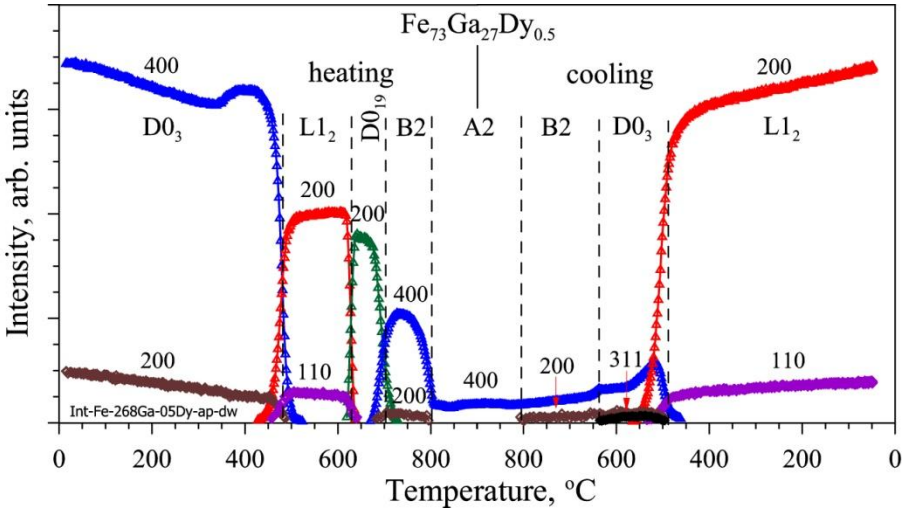

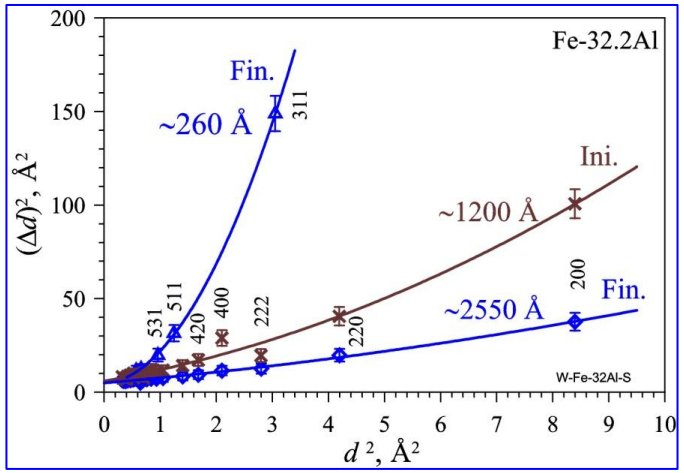

Peak width: *B*2 matrix + $D0_3$ clusters

Applied research: macroscopic stresses → shift of diffraction peak position

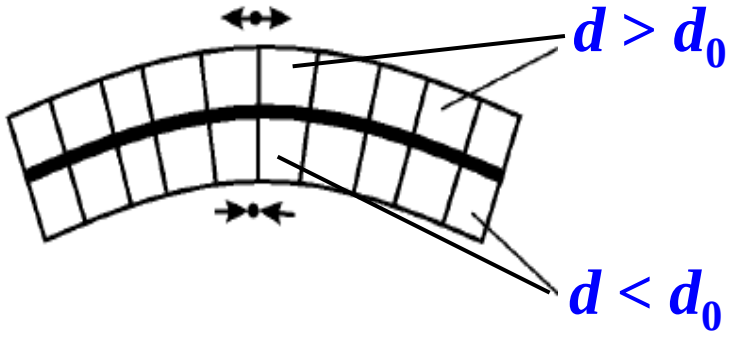

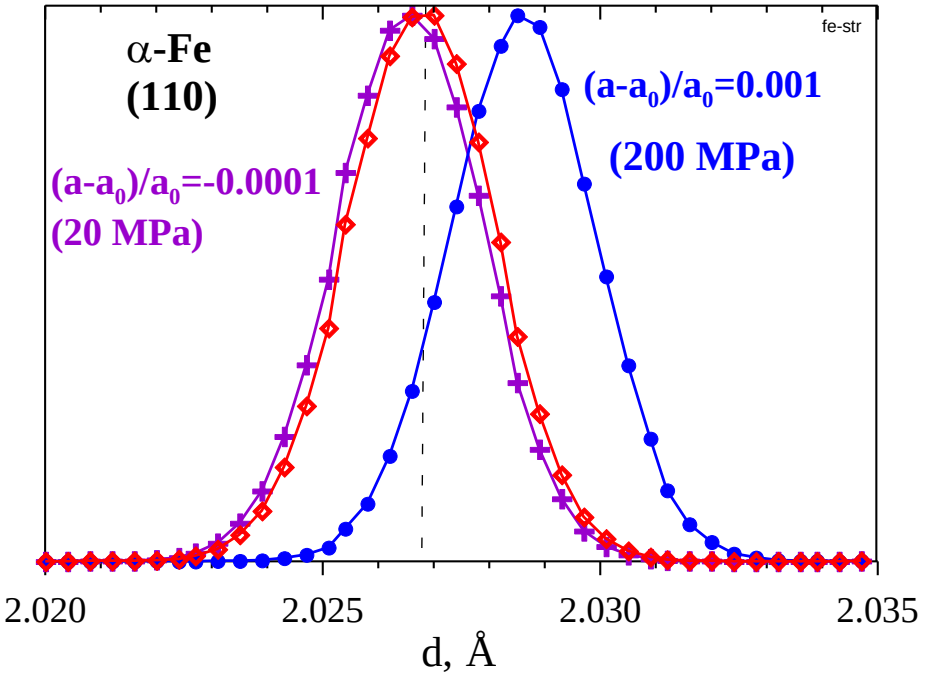

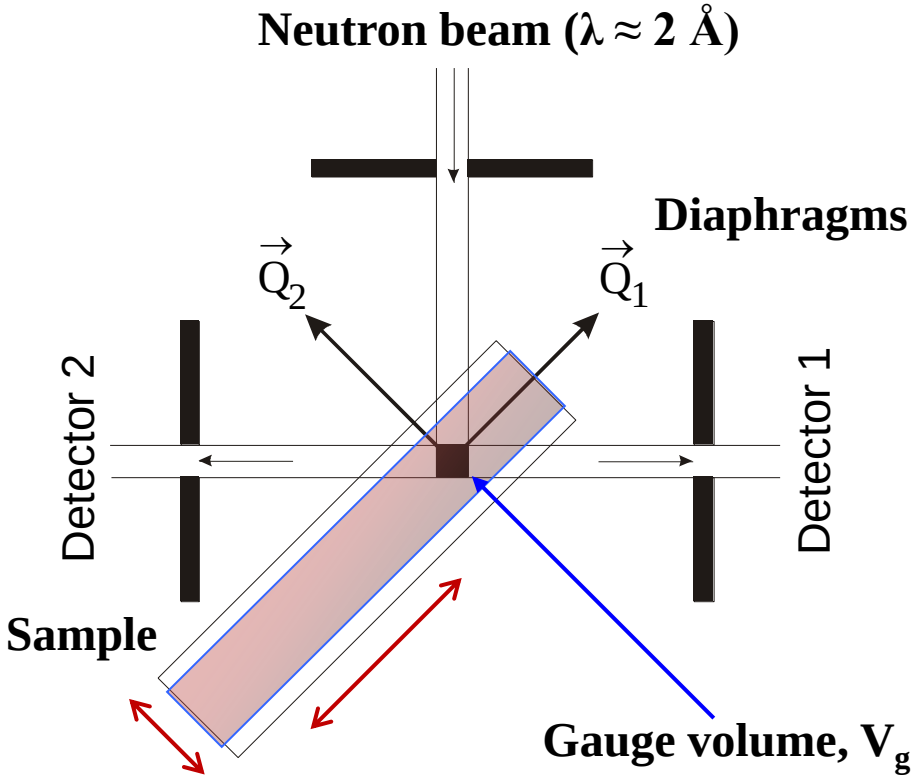

If ±90°-detectors are used, strans are measured In both directions Q_1 и Q_2 simultaneously.

Neutron diffraction study of residual stresses in perforator's striker

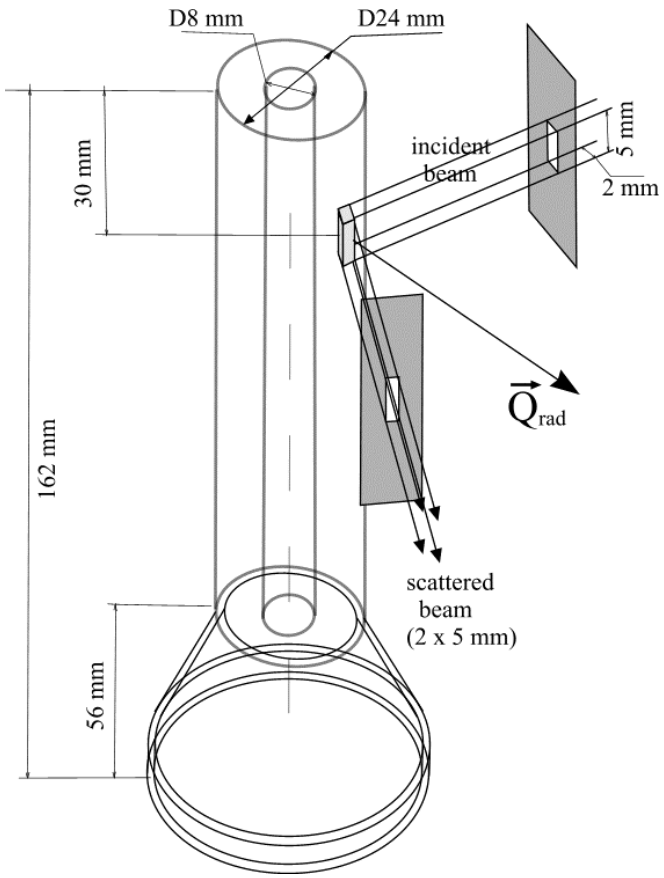

The layout of the experiment

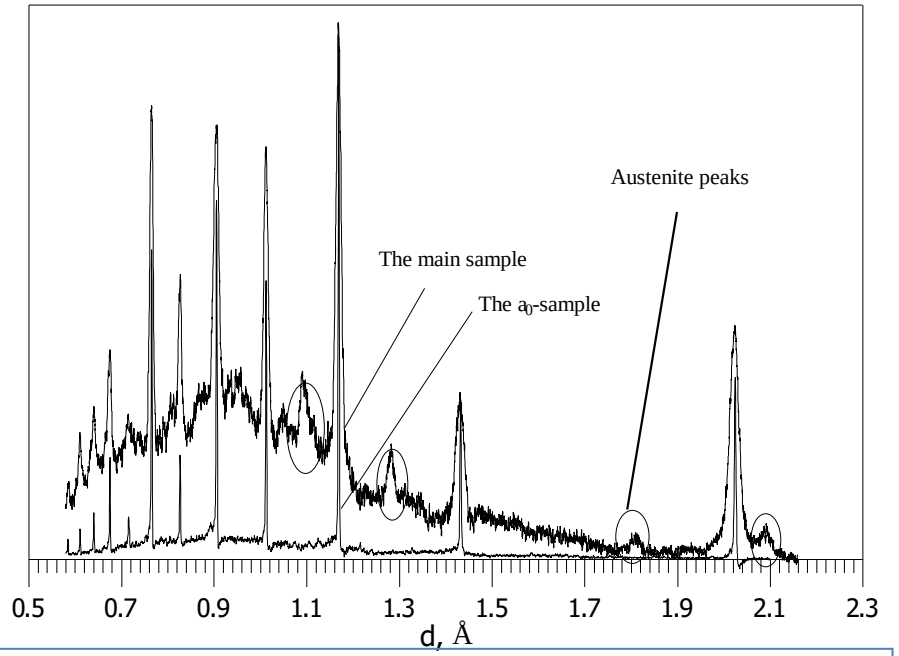

Comparison of neutron diffraction spectra from the sample before and after operation. The peak broadening as well as appearing of the austenite phase peaks are well pronounced.

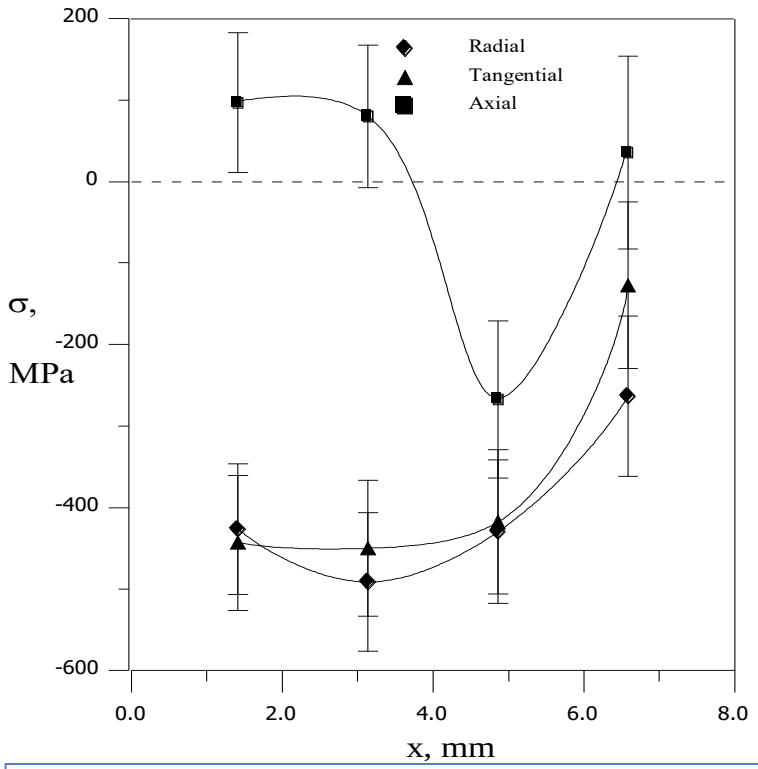

The measured residual stress distribution in the sample along radial coordinate *x*.

Rocks and minerals from Kola Superdeep Borehole, SG-3, *h* = 12 262 m

Mountains are always textured!

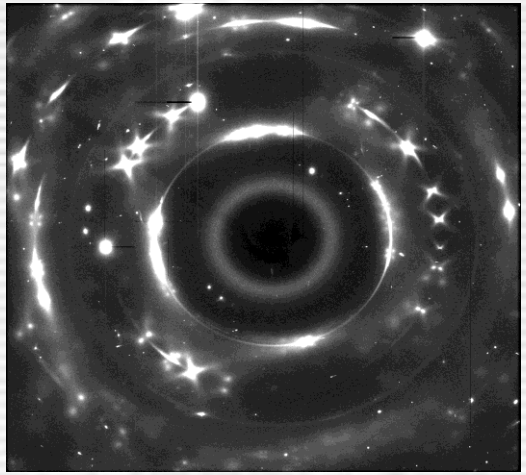

Debye-Scherrer rings

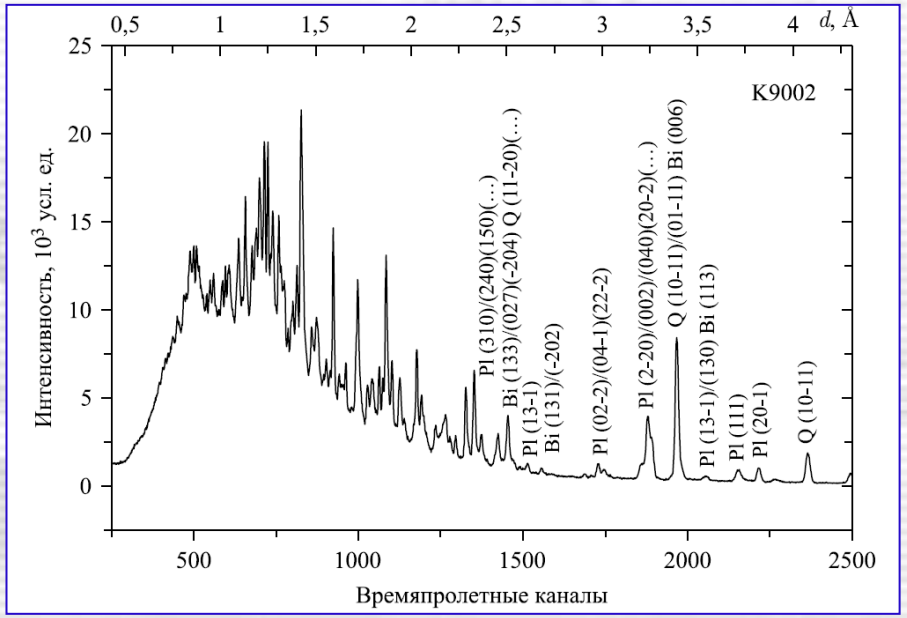

Spectrum of biotite gneiss , K9002 from SG-3. SKAT (IBR-2)

Musta-Tuntury suface
45 km from SG-3

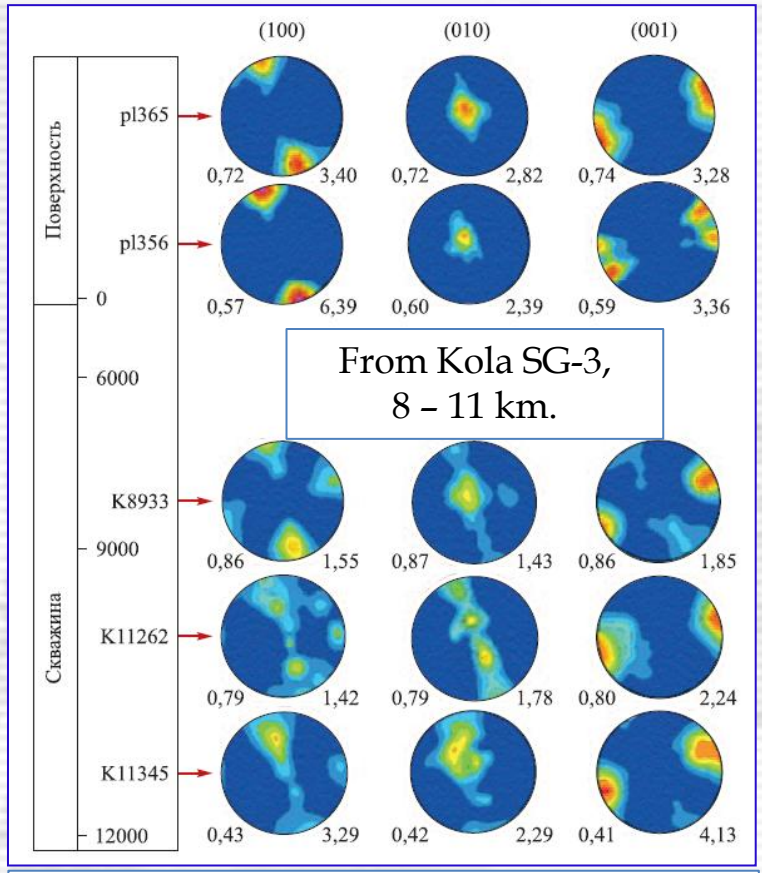

Pole figures of amphibolites from the surface and from SG-3

Main trends in neutron diffraction for condensed matter

Structural analysis: structures of increasing complexity, ≥ 50 parameters

Inclusion of coherent (Bragg) and diffuse scattering in the analysis

Increase in the speed of accumulation of diffraction data, $t_s \leq 10$ sec (down to 0.3 sec)

Increasing the range of simultaneously observed d_{hkl}, $0.3 \leq d_{hkl} \leq 30$ Å

Reducing sample volume, $V_s \leq 1$ mm^3, in high-pressure studies $V_s \approx 0.1$ mm^3

Analysis of the real structure (microstructure) of materials

At the IBR-2 reactor, all the above-mentioned trends are being implemented!

Many thanks to organizers of the NPRM-2025 conference!